A Retrieval Algorithm for Passive Microwave-Based Land Surface Temperature Considering Spatiotemporal Soil Moisture and Land Scenarios

Weizhen Ji, Yunhao Chen, Han Gao, and Haiping Xia

***Abstract*—Land surface temperature (LST) is an important parameter for the study related to land–air coupled systems. Satellite-based passive microwave (PMW) sensor is a significant approach to retrieving LSTs, which can penetrate the atmosphere conditions. However, soil moisture is one of the variables affecting PMW brightness temperature, yet few existing methods have considered it in the procedure of retrieving LSTs. On this basis, we propose a retrieval algorithm for PMW-based LST that comprehensively considers soil moisture changes and land scenarios (RA-PLST-SM) to take the soil moisture into account. Additionally, two fusion strategies one of which fuses the landform and soil moisture, and the other further fusing with land cover are proposed to construct the land environment description. Besides, we also propose a fusion strategy to integrate the LSTs from the time-interval-based models of month, quarter, and year. The mean root-mean-squared error (RMSE) referring to MODIS LSTs shows that RA-PLST-SM LSTs gain 3.13 and 2.32 K at day/night time. Also, referring to advanced LST data product, RA-PLST-SM LSTs present a yearly mean STD of 4.12 and 2.48 K at day/night time. Furthermore, the metric results according to six in situ stations demonstrate that RA-PLST-SM LST is significantly enhancing the consistency of actual LSTs, obtaining a mean RMSE of 4.42 K/3.48 K at day/night time. Moreover, the LST fusion strategy proposed in this article can effectively improve the quality of results. The progress of this article can promote the research fields to acquire cloudy LSTs and even provide the technique reference for PMW-based LST retrieval.**

***Index Terms*—AMSR2, land surface temperature (LST), MODIS, passive microwave (PMW) remote sensing, soil moisture (SM).**

I. Introduction

LAND surface temperature (LST) is a crucial variation for understanding the land–air coupling relationships [1], [2], facilitating the strategy to cope with global warming conditions. Hitherto, many studies have considered LST as an important indicator in further analysis of interaction among evapotranspiration [3], precipitation [4], heat flux [5], disaster events [6], [7], [8], [9], etc., developing great progresses to reveal land–air inherent rules. Consequently, acquiring the accurate LST dataset is significant for improving research precision on land energy exchange [10].

Combining satellite-based thermal infrared remote (TIR) sensing and retrieval algorithm is a common approach to obtaining LST, yet the cloud constrains its availability in many regions [11]. Thermal infrared sensors have an intuitive relationship with the thermal motion of surface molecules; hence, such sensors are widely used in the inversion of LST [12]. Three modes of retrieval algorithms have often been employed to compute LST, including single-channel mode [12], [13], multichannel mode [14], [15], and emissivity and LST separation mode [16]. Nevertheless, a cloudy sky is a severe challenge for TIR signal reception because the spectral range of TIR does not penetrate thick atmosphere conditions, such as rain or cloud cover; hence, over 67% of pixels are lost per year in MODIS LST products [17], which heavily restricts the thermal monitoring of land surface.

By contrast, passive microwave (PMW) sensors can penetrate cloudy sky to probe the land surface brightness temperature (BT) with weak attenuation of signal. Up to now, three methods can achieve PMW LST retrieval, including the physical, semiempirical, and empirical methods [18]. The physical methods have a solid theoretical basis and are capable of interpreting the retrieved LST results in terms of the radiative transfer equation (RTE). Even so, solving the RTE is extremely challenging because the equation systematically describes the transfer of radiation through the Earth's land–air system. Many physical variables need to be involved to compute the LST from the equation, yet some of the variables are also hard to gain [19]. Due to the complicated computing process, adopting semiempirical methods to estimate the LST is also a retrieving way, whereas such methods often do not consider the influence of the atmosphere and environment. Unlike the two methods above, the empirical method becomes a significant method that retrieves the LST by establishing an empirical equation between PMW channels and referenced LST. Furthermore, two advantages are presented in this method, including avoiding intricate computing processes as much as possible in RTE; and the physical meaning of retrieved LST is

Manuscript received 5 June 2024; revised 8 July 2024; accepted 20 July 2024. Date of publication 23 July 2024; date of current version 13 September 2024. This work was supported in part by the National Natural Science Foundation of China under Grant U23A2018, Grant 42171316, and Grant 72171128, and in part by the Beijing Laboratory of Water Resources Security. *(Corresponding author: Yunhao Chen.)*

Weizhen Ji and Han Gao are with the State Key Laboratory of Remote Sensing Science, Faculty of Geographical Science, Beijing Normal University, Beijing 100875, China (e-mail: wison@mail.bnu.edu.cn).

Yunhao Chen is with the State Key Laboratory of Remote Sensing Science, Faculty of Geographical Science, Beijing Normal University, Beijing 100875, China, and also with the Beijing Key Laboratory of Environment Remote Sensing and Digital Cities, Beijing Normal University, Beijing 100875, China (e-mail: cyh@bnu.edu.cn).

Haiping Xia is with the Institute of Remote Sensing and Earth Sciences, Hangzhou Normal University, Hangzhou 311121, China.

Digital Object Identifier 10.1109/JSTARS.2024.3432770

similar to TIR-based LST, which promotes the fusion process of both two-sensor data to generate all-weather LST dataset.

To ensure the accuracy of LST, regressed empirical equations often need to be built independently on different environmental conditions. Most scholars work on two aspects of empirical approaches: channel selection [20], [21], [22] and scenario optimization [18], [23], [24]. Exploring suitable channels as well as polarizations for LST retrieval is the main strategy of channel selection. For instance, McFarland et al. [20] proposed that higher frequency channels (e.g., the horizontal and vertical polarized BT approximately channels 37 or 89 GHz) are more sensitive for LST retrieving. For scenario optimization, Owe and Van De Griend [25] employed McFarland's algorithm to regress the model on day/night time in each season. Zhou et al. [18] further adopted the land cover to divide the scenario, which detailed the regressed model. Subsequently, Zhang and Cheng [23] fused topography into the land cover to refine the scenarios based on Zhou's method. Overall, the previous studies have already drawn the land scenarios via land cover and topography. Even though these efforts have brought much progress in retrieving PMW LST, some issues still need to be figured out. First, PMW channels are presented that have a strong relationship with soil moisture (SM) due to the higher moist land varied dielectric constant [16], [20], [26], whereas few studies consider the SM changes in scenario classification according to our knowledge. Furthermore, SM is an essential factor that affects skin temperature through sensible and latent heat fluxes [27], [28]. Thus, it is necessary to apply this land variable in LST retrieval. Second, previous studies only adopted intrayear variables of landform and land cover to establish the all-weather regress model, the accuracy may remain unstable due to each scenario changing per day. Third, how to couple the dynamic SM changing into the description of the land environment is still not clear. Therefore, establishing a dynamic scenario taxonomy that further considers landform, land cover, and the changes in SM is necessary for retrieving scientific and reasonable PMW-based LSTs.

In this article, we proposed a retrieval algorithm for PMW-based LST that comprehensively considers soil moisture (RAPLST-SM) changes and the land scenarios and further propose two strategies for achieving the coupling process and a multi-spatiotemporal fusion strategy which better couple the different regression models. The main objective of this study is given as follows:

1) to develop a retrieval method for PMW LST with higher accuracy;
2) to explore the feasible fusion strategies on both land environment description and coupling among regression models;
3) to verify the effectiveness of incorporation considering landform, SM, and land cover simultaneously.

The results show that the utilization of SM can make an accuracy improvement in the retrieval techniques of PMW LSTs. Also, the results of this study will inform subsequent studies or directly facilitate research precise for related fields.

II. Study Area and Data Processing

A. Study Area

This article selects China's landmass as a study area to retrieve and validate PMW LST from satellite AMSR2. We selected this area for three reasons.

1) The region of China's landmass covers a wide range of land surface types and diverse geomorphology.
2) With the rapid development of China's economy, the frequent occurrence of climate disasters in recent years has become a constraint on the harmonious coexistence of human nature.
3) China's landmass is subject to severe cloud cover, especially in central, southern, and eastern China, which suffers from prolonged cloudy skies every year.

The detailed location and geographical condition of the study area are shown in Fig. 1.

B. Data and Processing

1) Satellite Data: MYD11A1 MODIS L3 LST product from the National Aeronautics and Space Administration[1] is used to construct the regress model. We adopt the Aqua-based MYD11A1 LST product as the reference temperature because it approximates the orbital time of AMSR2 PMW sensors [24]. We acquire the data during March 2019–March 2020. Each LST image has attached a quality control that retains the accuracy of pixels less than 1 K with a "Good Quality" label over the homogeneous surface [29]. All the collected MODIS LST will be upscaled to 25 km by aggregation method. In addition, this article used the MCD12Q1 level 3 land-cover product to achieve the fusion on which the IGBP system was based, covering a comprehensive range of land-use types with an accuracy of 75% [30]. This product is generated via Terra and Aqua to synthesize one land-cover image per year, which contains 12 natural vegetation land types and 5 nonvegetation types. The MCD12Q1 level 3 land-cover data are upscaled via a slide window method, which will be explicitly illustrated in Section III-B. However, such a product can provide only one image data per year, which does not measure the daily changes in vegetation phenology. Considering this issue, we acquired normalized difference vegetation index (NDVI) from MYD13Q1 16-day synthetic product to compensate for the annual increase and decrease of the vegetation. Besides, we also adopt MYD10C1 level 3 snow cover product to further describe the regions of ice and snow. We adopt the aggregation method to upscale NDVI and snow cover to 25 km. The information list of used data in this article is illustrated in Table I.

AMSR2 is a microwave sensor onboard satellite GCOM-W1, which provides two-time daily (local time approximately 1:30 A.M. and 1:30 P.M.) land observation. This satellite started in orbit in 2012 and provided seven channel data (6.9, 7.3, 10.7, 18.7, 23.8, 36.5, and 89 GHz) with two modes of polarization, horizontal and vertical. The level 3 AMSR2 BT with the resolution of 25 km is adopted to retrieve LST, where the data can

[1] [Online]. Available: https://www.earthdata.nasa.gov/

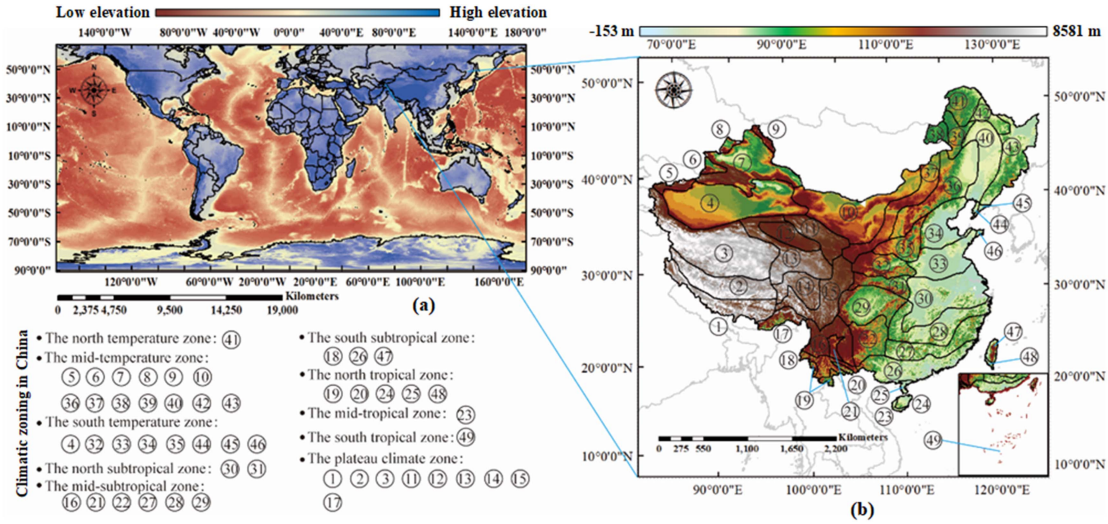

Fig. 1. Geographic condition and region of the study area. (a) Location of China on a global scale. (b) Explicit conditions of China's landmass.

TABLE I
INFORMATION OF THE DATA USED IN THIS ARTICLE

Data sources	Variable names	Abbreviation	Temporal resolution	Spatial resolution
MYD11A1 MODIS L3 LST product	Land surface temperature	LST	Daily	1 km
MCD12Q1 level 3 land-cover product	Land cover	LC	Yearly	500 m
MODIS MYD13Q1	Normalized difference vegetation index	NDVI	16 days	250 m
MYD10C1 level 3 snow cover product	Snow cover	SC	Daily	500 m
The level 3 AMSR2 brightness temperature	AMSR2 BT	BT	Daily	25 km
The SRTM	Digital elevation model	DEM	—	30 m
SMCI 1.0	Soil moisture data	SM	Daily	1 km
LIGGD	The desert map of China	Desert	—	—
TRIMS LST	Thermal and reanalysis integrating moderate-resolution spatial-seamless LST	TRIMS LST	Daily	1 km
HiWATER	In situ measurements	AROJ, DAM, DSL, HL, HMO, HZZ	Intra-hourly	—

be accessed via the Japan Aerospace Exploration Agency.[2] The data collection time span is the same as MODIS LSTs.

The shuttle radar topography mission (SRTM) provides the data of a digital elevation model (DEM) with two spatial resolutions of 1″ and 3″, covering Earth's surface between 60°N and 56°S, which is approximately 80% global land surface area. The resolution of 3″ is adopted in this work because it is presented with better accuracy than 1″ across China [31]. In this article, the DEM data are upscaled to 25 km via aggregation, which matches the AMSR2 PMW BT.

2) SM Data: The daily SM data product of SMCI 1.0 [32] is used in this article to describe the daily changes in land moisture. This product is provided by the National Tibetan Plateau/Third Pole Environment Data Center,[3] generated by the China Meteorological Administration 1648 stations with ten-layer depth SM as benchmark data. Simultaneously, adopting the leaf area index, land-cover types, ERA5-land reanalysis data, terrain, and soil properties as covariates, we reconstruct the daily SM dataset via a machine-learning model [33]. The data were also upscaled to 25 km by aggregation.

3) Desert Distribution Data: Due to the land thermal characteristic of the desert region being different from other land conditions, we acquire the desert distribution map of China [34]

[2][Online]. Available: https://suzaku.eorc.jaxa.jp/GCOM_W/index.html

[3][Online]. Available: https://data.tpdc.ac.cn/

TABLE II
DETAILS OF THE SIX SELECTED IN SITU GROUND STATIONS

Station	Latitude and Longtitude (°N, °E)	Elevation (m)	Height (m)	Surface type	Time span
Arou (AROJ)	38.05, 100.46	3033	5	Grasslands	2019.3–2020.3
Daman (DAM)	38.86, 100.37	1556	12	Croplands	2019.3–2020.3
Dashalong (DSL)	38.84, 98.94	3739	6	Grasslands	2019.3–2020.3
Huailai (HL)	40.35, 115.79	480	5	Croplands	2019.3–2020.3
Huangmo (HMO)	42.11, 100.99	1054	6	Barren	2019.3–2020.3
Huazhaizi (HZZ)	38.77, 100.32	1735	6	Barren	2019.3–2020.3

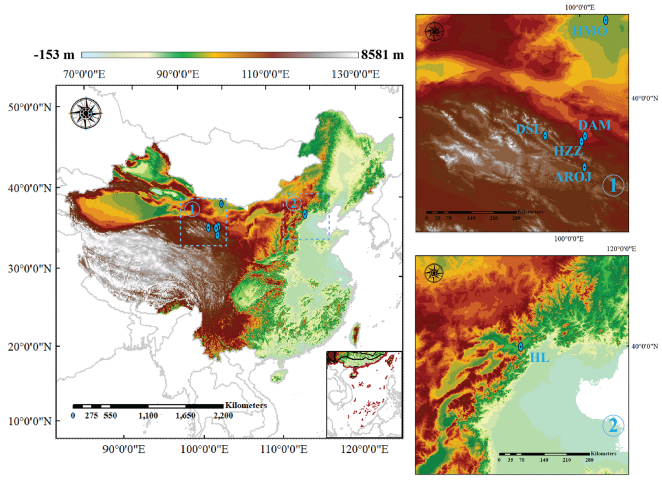

Fig. 2. Location of six in situ stations.

via a big Earth data platform for three poles.[4] Additionally, LIGGD contained nine desert areas across China's landmass.

4) LST Data Product: For validating the precise of all-weather conditions, we further compared retrieved LST with TRIMS LST data product (2000–2020, acquired via the available website[5]), which was generated by Zhou et al. [35], [36], [37], [38], [39] via TIR-based RTE, and was a greater LST production that has supported numerous thermal monitoring research. The standard deviation of bias (STD) of this product is 1.45 and 1.17 K for daytime and nighttime. This dataset will be upscaled to 25 km via aggregation.

5) Meteorological Station Data: To evaluate the accuracy of retrieved LSTs, we collected six in situ measurements (i.e., upwelling and downwelling longwave radiation) from Heihe River Basin [40], [41], including Arou (AROJ), Daman (DAM), Dashalong (DSL), Huailai (HL), Huangmo (HMO), and Huazhaizi (HZZ). The detailed information on these stations is shown in Table II, and the locations of these stations are shown in Fig. 2.

According to the Stefan–Boltzmann law, the in situ LST can be computed through the upwelling and downwelling longwave radiation, and the equation is given as follows:

$$\mathrm{LST\_in{-}situ} = \left[\frac{R_{\mathrm{up}} - (1-\varepsilon b)\, R_{\mathrm{down}}}{\sigma \varepsilon b}\right]^{1/4} \tag{1}$$

where R_{up} and R_{down} are the upward and downward longwave radiations in Wm^{-2}; ε_b is the broadband emissivity, which is computed from the narrowband emissivity from MODIS MYD11A1 through the approach of Liang [42]; and σ is Stefan–Boltzmann's constant, which is set as 5.67×10^{-8} $\mathrm{Wm}^{-2}\mathrm{K}^{-4}$ [43].

III. METHODS

A. Physical Principle of the RA-PLST-SM Retrieval Algorithm

The primary theoretical basis for our experiments is derived from the PMW-based RTE. After the derivations, we find that the surface temperature retrieval is correlated with six land variables. First, satellites that receive microwave signals involve the radiation components from the surface/subsurface land, the near-surface atmosphere, and the upper atmosphere. Thus, the BT can be described by the following equation:

$$R_p(T_{bp}) = \tau_p(\theta) e_p R_p(T_s) + (1-e_p)[1-\tau_p(\theta)]\tau_p(\theta) \times R_p(T_{\mathrm{down}})_{+[1}\, - \tau_p(\theta)]R_p(T_{\mathrm{up}}). \tag{2}$$

Among the variables in this equation, $R_p(T_{bp})$, $R_p(T_s)$, $R_p(T_{\mathrm{down}})$, and $R_p(T_{\mathrm{up}})$ are the radiation-perspective variables, where the former two ones are the received radiation of the satellite ($\mathrm{Wm}^{-2}\mathrm{sr}^{-1}\mathrm{Hz}^{-1}$), respectively, from the components of BT and surface temperature, and the last two ones indicate the radiations of downward and upward equivalent temperature; $\tau_p(\theta)$ represents the atmospheric transmittance; e_p is the emissivity from the land; p is the frequency of PMW channels; and θ is the view angle. Completing the perspective transformation from radiation intensity to temperature is critical to solve the LST. Based on this, according to Planck's laws, the radiation intensity at one frequency is equal to the electromagnetic radiation emitted by a blackbody at a given temperature T, as follows:

$$R_p(T) = \frac{2kp^3}{c^2(e^{kp/vT}-1)} \tag{3}$$

where $R_p(T)$ is the radiation intensity; k represents Planck's constant; p is the frequency; c is the light speed, and e represents the natural constant; and v is Boltzmann's constant. Adopting Taylor's formula to expand the Plank equation can simplify the

[4][Online]. Available: http://poles.tpdc.ac.cn/en/data/4999860d-734b-478f-bfbb-10b673ad63fe/

[5][Online]. Available: https://data.tpdc.ac.cn/en/data/05d6e569-6d4b-43c0-96aa-5584484259f0/

denominator as follows:

$$R_p(T) = \frac{2nTp^2}{c^2} \frac{1}{1+(kp/vT)+(kp/vT)^2+\cdots+(kp/vT)^n}. \tag{4}$$

Thus, the half partial of the equation can be negligible in accordance with the Rayleigh–Jeans approximation. Then, the original Planck's equation can be reduced to the following approximate form:

$$R_p(T) \approx \frac{2nTp^2}{c^2}. \tag{5}$$

After the transformation, the RTE can express the transmittance via the perspective of temperature as follows:

$$T_{bp} = \tau_p(\theta)e_pT_s + (1-e_p)[1-\tau_p(\theta)]\tau_p(\theta)T_{\text{down}} + [1-\tau_p(\theta)]T_{\text{up}}. \tag{6}$$

Obviously, the LST T_s demonstrates a close relationship with five physical variables of T_{bp}, $\tau_p(\theta)$, e_p, T_{down}, and T_{up}. The existing studies have illustrated that all of these parameters can be characterized via surface properties (such as topography and land cover) as well as time and space. Of them, the emissivity e_p is a significant parameter to retrieve LST in RTE because it directly affects the reflection properties of the underlying surface [16]. In general, two factors are related to the change in the emissivity: terrain texture and moisture content, where the former is described by topography and land cover, whereas the moisture is less to be considered in the classification of underlay types. According to the RTE, e_p and soil reflectivity satisfy the following equation:

$$e_p(\theta) = 1 - \Gamma_p(\theta) \tag{7}$$

where $\Gamma_p(\theta)$ is the soil reflectivity with the view angle θ. Then, the soil reflectance for horizontal and vertical polarization (Γ_{pH}, Γ_{pV}) in each channel can be calculated as follows:

$$\Gamma_{pH} = \left|\frac{\cos\theta - (\varepsilon - \sin^2\theta)^{1/2}}{\cos\theta + (\varepsilon - \sin^2\theta)^{1/2}}\right|^2,$$
$$\Gamma_{pV} = \left|\frac{\varepsilon\cos\theta - (\varepsilon - \sin^2\theta)^{1/2}}{\varepsilon\cos\theta + (\varepsilon - \sin^2\theta)^{1/2}}\right|^2 \tag{8}$$

where ε is the dielectric constant that needs to be ensured in accordance with the material and moisture content of the ground surface. In consequence, the functional correlation between LST and BT can be illustrated in the following formula:

$$T_s = f(T_{bp}, \text{Topography}, \text{SM}, \text{Landcover}, \text{time}, \text{space}) \tag{9}$$

where f denotes the equation for retrieving the LST.

For the regressed model, we use seven channels to establish the algorithm to retrieve the LST. At the same time, we also adopt two terms that included the difference between the vertical polarization of 36.5 and 18.7 GHz, and the vertical polarization of 36.5 and 23.8 GHz into the equation, which may compensate for the influence of agriculture moist soil and atmosphere water vapor [20], respectively. Finally, the equation, which is used to retrieve the LST, is given as follows:

$$T_s = C_0 + \sum_{i=1}^{7}(C_{ih}T_{pih} + C_{iv}T_{piv}) + D(T_{p36.5v} - T_{p18.7v})^2 + E(T_{p36.5v} - T_{p23.8v})^2 \tag{10}$$

where C_0, C_i ($i = 1, 2, \ldots, 7$), D, and E are the coefficients of each term; the subscripts h and v represent the horizontal and vertical polarizations of the PMW channel, and i denotes the frequencies of AMSR2. To better make a comparison to prior studies, we adopted a linear model to compute the coefficients of the equation. Three assessment metrics are employed to estimate the performance of the proposed model, including root-mean-squared error (RMSE), determination coefficient R^2, mean bias error (MBE), and standard deviation of bias (STD). In addition, we use a density equation to estimate the dispersion degree of spatial points; the equation is given as follows:

$$\text{Density} = \left[\frac{1}{\text{Mean}(\text{DistanceNeighbors})}\right] \tag{11}$$

where Mean denotes the average result of all neighbor points, and $\text{Distance}_{\text{Neighbors}}$ represents the Euclidean distance of a traversal point from surrounding points.

B. Construction of the RA-PLST-SM

The procedure of RA-PLST-SM consists of five parts, including the independent procedures of topography, SM, and land cover; the construction of RA-PLST-SM containing the fusion of topography–SM, and the further incorporation with land cover and the other relative land variables; and the retrieval method of PMW LST. The entire flowchart is shown in Fig. 3.

1) Classification of Topography: In this article, we adopt the altitude and topography relief [44], [45] to achieve the division of basic landform, which refers to Zhang and Cheng's article [23]. In China's landmass, we classify the image by altitude into three categories: low altitude (DEM $<$ 300 m), middle altitude (300 m $\leq$ DEM $<$ 2800 m), and high altitude (2800 m $<$ DEM). At the same time, the topography relief is divided into four classes, where the DEM less than 270 m is determined to the plain; the DEM between 270 to 1000 m and 1000 to 2300 m is defined as hill and moderate mountain, respectively; the DEM higher than 2300 m is the steep mountain. After that, we use a sliding window with a size of 5 $\times$ 5 to determine the basic landform; the results are shown in Fig. 4.

2) Fusion of Topography and SM: Four types of SM are determined in this article to further describe the land condition to retrieve the LST, including dry soils, slightly moist soils, moist soils, and extremely moist soils. At first, we resample the daily 1 km SM data to 25 km, which matches the topography resolution. To ensure the boundary of each class, we employed the K-means clustering algorithm to process each SM image, which attempts to obtain the suitable decision values (as shown in Fig. 3). After this step, we found that there is a slight fluctuation existed in per class during one year, to which adopts the mean value of each class to segment the SM. The criteria of every class contain 0 $<$ 0.121, 0.121 $\leq$ SM $<$ 0.263,

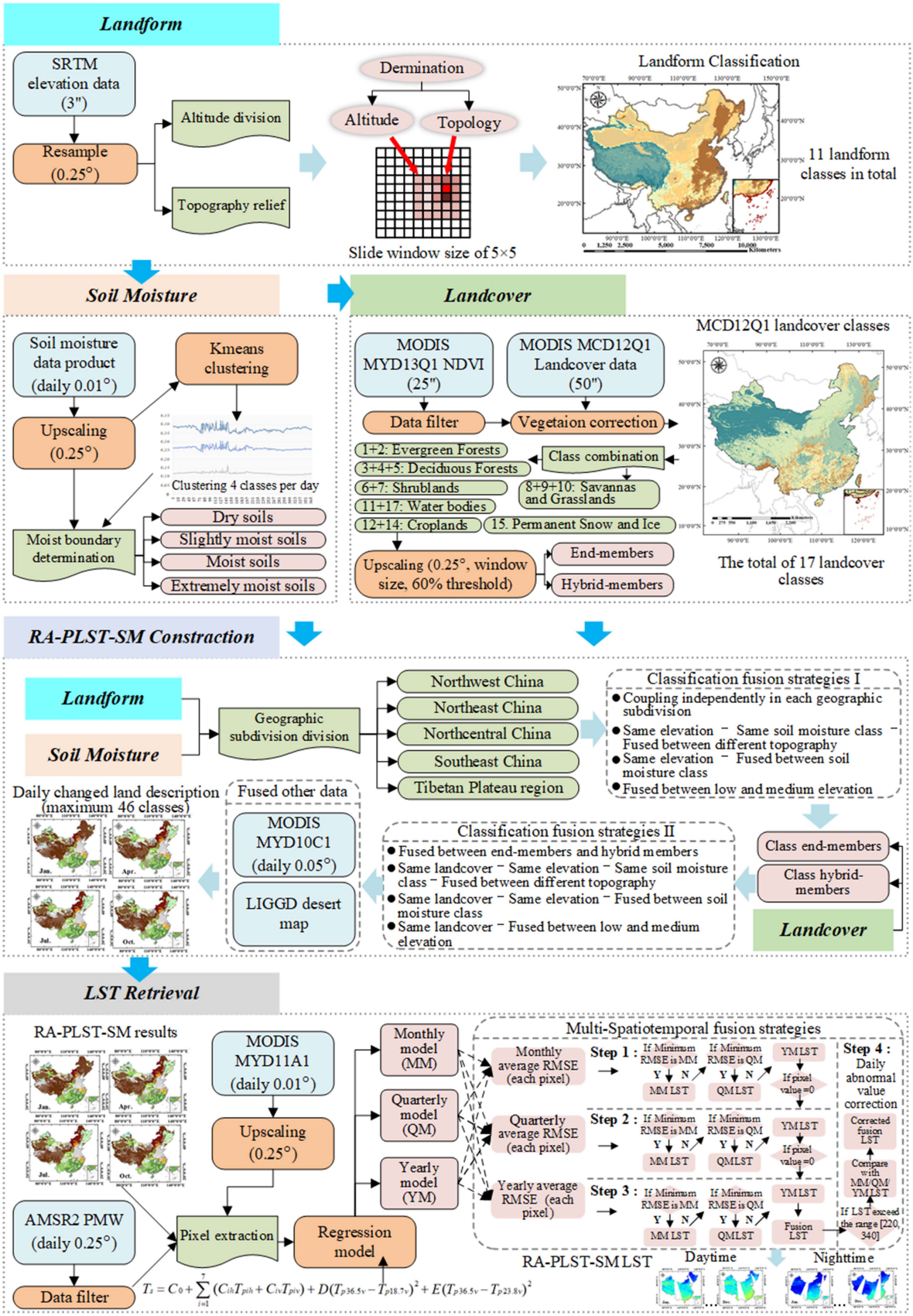

Fig. 3. Flowchart of dynamic RA-PLST-SM construction and corresponding fusion strategies.

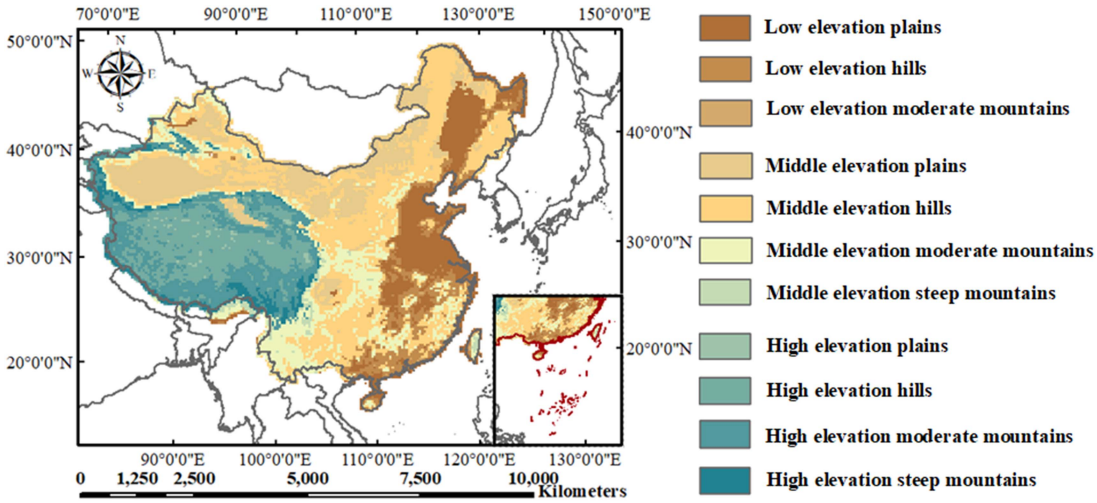

Fig. 4. Diagram of the landform, containing 11 categories in total.

$0.263 \leq \text{SM} < 0.374$, and $0.374 \leq \text{SM}$ (unit: m^3/m^3), where all of these intervals correspond to the four categories illustrated above. And then, we adopt this classified boundary to complete the division of SM.

Regarding the fusion between the topography and the SM, we propose a four-step strategy to achieve this process. Since factors, such as latitude, topography, and coastal inland, produce unique characteristics of the land temperature, achieving the fusion with the results of SM classification for the entire study area may allow the regression model amidst the turbulent fluctuation of BT to complete the LST retrieval. Considering the diversity of different regions in the study area, we divide the whole study region into Northwest China, Tibetan Plateau region, Northcentral China, Southeast China, and Northeast China, respectively, depending on the distribution of SM and topography from west to east of China's landmass. Subsequently, we further optimize the piecemeal pixels and regions with similar attributes through the fusion strategy to extract an adequate sample size to train the regression model. All of these fusion steps are utilized for two goals of smooth piecemeal pixels and reduce the fused classes. The detail of these steps is shown in Fig. 5.

After that, the fusion results containing 38 classes are obtained via the fusion strategy. Due to the land cover being an important factor for the land emissivity as well, we further propose a strategy to couple the topography–SM with the land cover.

3) Further Fusion With Land Cover: Land cover is directly related to the pattern and variation of land surface thermal environment. However, the usual land-use cover data allow for a one-phase per year through the accumulation of categories on the surface. If the 365 days are shared in one land-cover result, it will not be possible to consider category turnover with time, especially the vegetation phenology. For this reason, the MODIS MCD12Q1 product is used as the basic land-cover data, and we employ the MYD13Q1 NDVI product to try to correct this phenomenon. First, we employ a changing-weight filter method [46] to reconstruct high-quality NDVI data, which denoises the original data product. Afterward, the time-domain interpolation was applied to expand the synthetic NDVI product every 16 days to the daily. Finally, we corrected the land cover via the process of replacing the value with none, which referenced the NDVI daily data.

Before implementing the fusion, spatial resolution likewise needs to be integrated into one scale for the two data. Here, we reproduce the aggregation-based upscaling method of Zhou et al. [18] to upscale the NDVI product from 1 to 25 km. In this method, each pixel in a 25 km scale will correspond to 625 pixels in 1 km; thus, if one land-cover class occupied pixels over 60% of these, 625 pixels will be regarded as an end member for this class, otherwise hybrid member (the threshold of 60% is proved to be the best value in the work of Zhou et al.). The aforementioned process is achieved via a sliding window with a stride of 1. Eventually, we also propose a four-step strategy to incorporate corrected land cover into the daily results of topography–SM. The explicit content is illustrated in Fig. 6.

End-member and hybrid-member pixels are two crucial units related to pixel representation. In consequence, we first divide these two types of units, and then further fuse the land cover into the results obtained from the previous step. After that, the scattered independent classes will find it hard to extract sufficient referenced MODIS LST, thus affecting the abnormal data in the retrieved results. With regard to this situation, we combine these classes, which are less than 100 pixels into similar classes in accordance with SM and elevation.

Different time intervals will make the retrieval model show distinct performance, which requires a fusion strategy to couple the LST results of the models from which the time scales of monthly, quarterly, and annual are obtained. Hence, this article has a fusion strategy with four steps integrating each time-interval model. First, the monthly, quarterly, and annual models are unified to calculate the average RMSE with MODIS LST pixelwise based on the month scale. Then, each pixel uses the LST result of the model with the smallest RMSE among the three models. Second, if there are still zero-value pixels, the average RMSE of each model is calculated by quarter scale, and the model with the smallest RMSE result is used to fill the zero-value pixels. Third, if there are still existing no-data pixels,

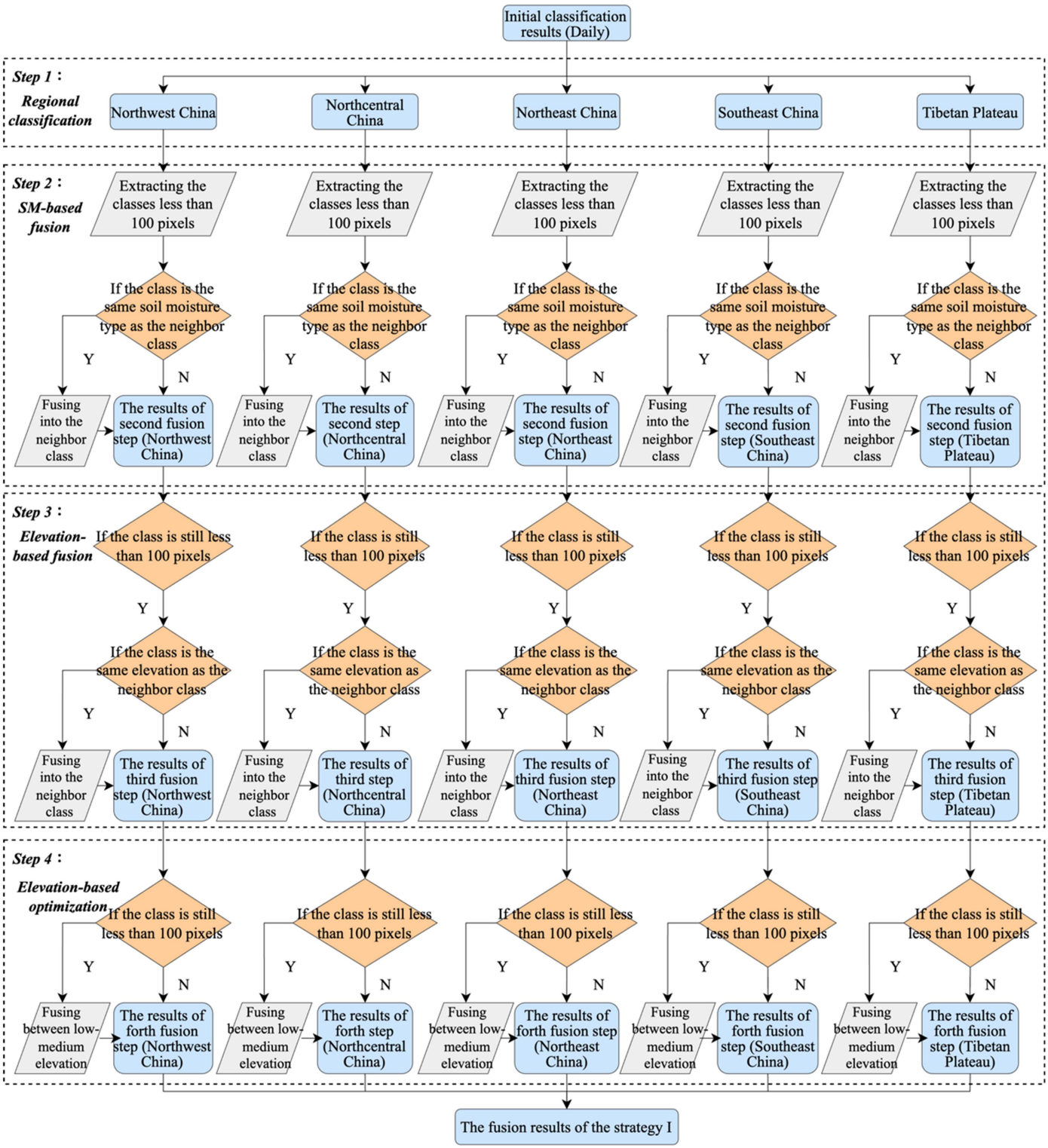

Fig. 5. Fusion strategy between the classification of landform and SM.

it is processed again in the same mode using the annual scale. Due to insufficient training samples in a smaller time-interval model, the procedure may pad "effective LST" into the final LST, thus impeding the subsequent steps to fill a portion of pixels as abnormal data. Consequently, fourth, for the outliers where the temperature exceeds the range of [220 K, 340 K], we will check the LSTs of the three models again and use their normal values to finish the compensation. The entire process is described in Fig. 7.

To describe the dynamic changing of the land scenario, snow cover and deserts can also cause surface and PMW BTs to take on unique properties. Therefore, this article adds these regions to

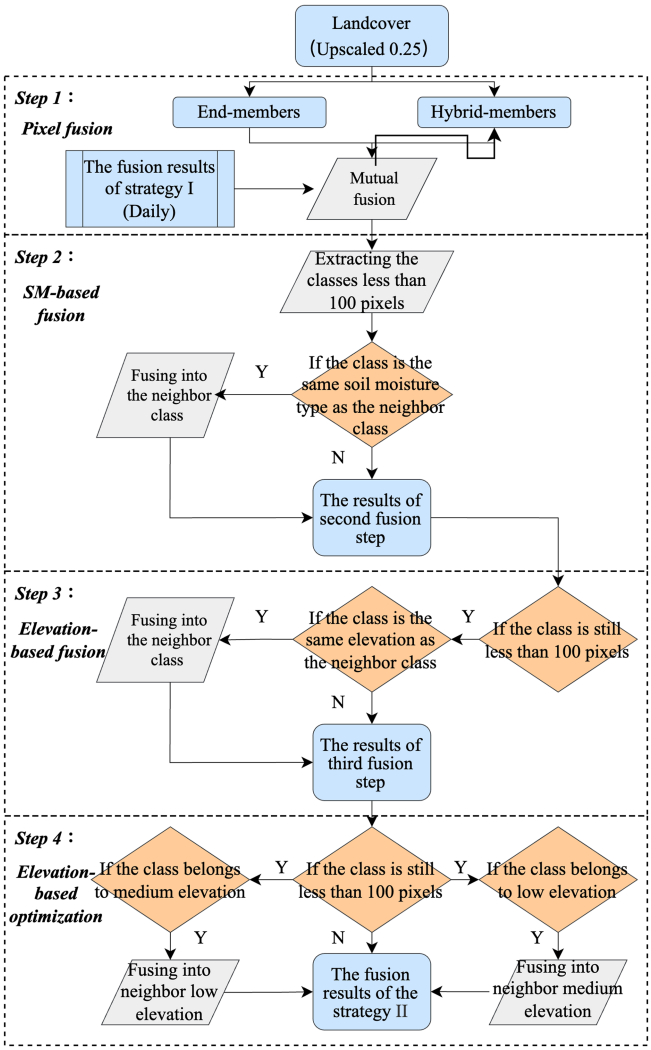

Fig. 6. Fusion strategy that incorporates the land cover into the fused classification between landform and SM.

the classification results through two products of MYD10C1 and LIGGD. Furthermore, we divide three classes, which include the desert regions in China's landmass of northwestern, northern, and northeastern. Finally, a dynamic class number is contained every day, where the number of categories per day fluctuates from 42 to 46. The results are shown in Fig. 8. To discuss the seasonal differences in the inversion results, in this study, March–May is designated as spring, June–August as summer, September–November as autumn, and December–February of the following year as winter.

IV. Results

A. Spatiotemporal Pattern of RA-PLST-SM LSTs

We provide the RA-PLST-SM LSTs of the 15th day of each month to show the spatial and temporal variation of China's landmass, as shown in Fig. 9. The results indicate that RA-PLST-SM LSTs can reflect the temperature changes in China's landmass regardless of daytime and nighttime. As for Northwest China, RA-PLST-SM LSTs demonstrate an apparent variation in large desert areas, which remain high temperature during spring–autumn and gradually decrease toward cold in winter. Besides, severe cold conditions are common on the Tibetan Plateau at night due to its higher altitude and long-term snow/ice cover. During the day, the temperature rises due to the large amount of solar radiation absorbed by the land surface. In addition, the Tibetan Plateau shows obvious seasonal changes both during the daytime and at nighttime. The Northeast region shows cold characteristics in autumn, winter, and early spring. The reason is that long-term snow cover is prone to occur at higher latitudes, which causes the surface temperature in the region to lag in the recovery in spring. The areas with relatively high temperatures throughout the year occur in central China, southern China, and eastern China. Especially in southern China, it has always maintained relatively high land temperatures compared with the other regions, especially in summer and autumn. Overall, RA-PLST-SM LSTs can reflect the spatiotemporal characteristics of surface temperature in China's landmass and also is an effective method to obtain PMW-based LST.

B. Assessments of RA-PLST-SM LSTs

1) Assessment Based on MODIS LST: Considering numerous studies adopted MODIS LST to test the accuracy of retrieved LST, this article also acquired these data to verify the RA-PLST-SM LST. First, we randomly selected 5% valid pixels from each day. The results show that the mean RMSE of RA-PLST-SM LST demonstrates 3.13 and 2.32 K in daytime and nighttime, and R^2 achieves 0.97 and 0.99 in daytime and nighttime, as shown in Fig. 10.

Moreover, the month with the largest RMSE occurs in June, indicating a strong temperature fluctuation in this month that impacts the model regression. Also, the results show a significant decrease in accuracy from March to August. Here, the reason for these occurrences may be the variable meteorological changes during spring and summer that affect the performance of the regression model. In other words, the land surface absorbs solar radiation in spring and summer is undoubtedly higher than in the other two seasons. Consequently, a more energy transfer between radiation and temperature increases surface heat storage and further intensifies land–air energy balance. A diverse land environment will disturb the original temperature profile and cause the presentation of land heat to be confused. Therefore, this situation brings a great challenge for the retrieval model, which is the main reason for the seasonal variation of RA-PLST-SM.

As for the nighttime, the higher MBE often appears in the winter in which the fluctuation characteristic of LST is different from the daytime. Meanwhile, the bias trend between RA-PLST-SM LST and MODIS LST from the nighttime is opposite to the daytime; more explicitly, there is less bias fluctuation from May to August. The reason for this phenomenon is that the solar strikes the ground for a longer time in the summer, causing the surface to have a higher rate of heat storage, and then the heat energy releasing to the near-surface air temperature at night, making a less difference in terms of land–air temperature under various land environments. However, for the spring, autumn, and

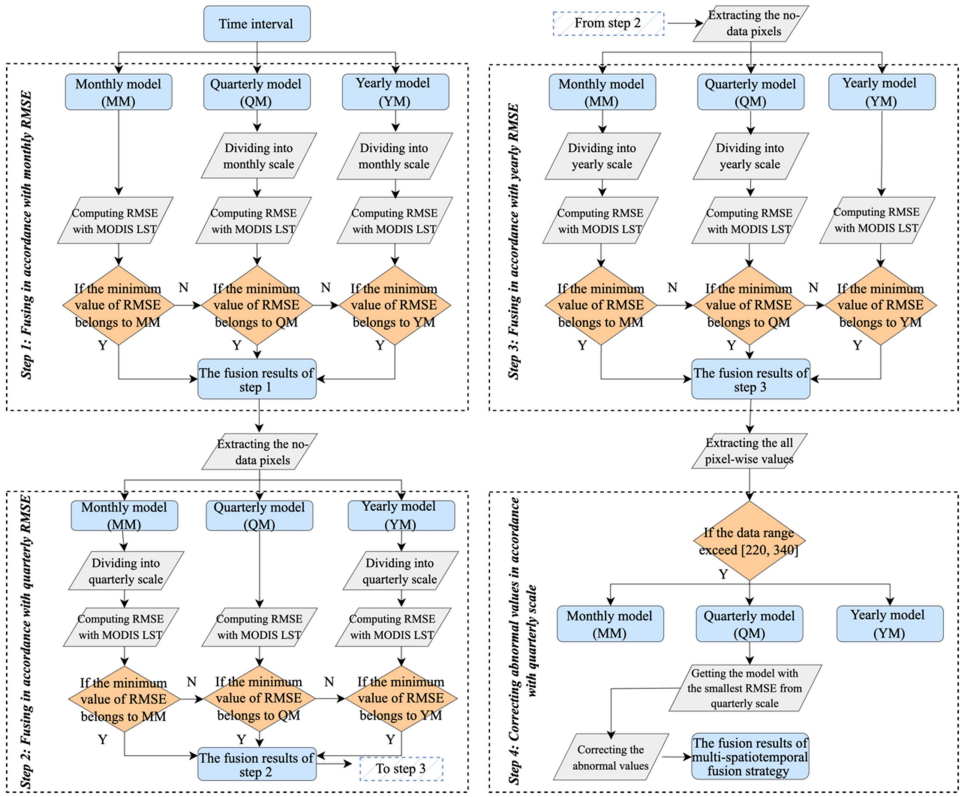

Fig. 7. Streamlining of the four-step fusion strategy that incorporates each time-interval model.

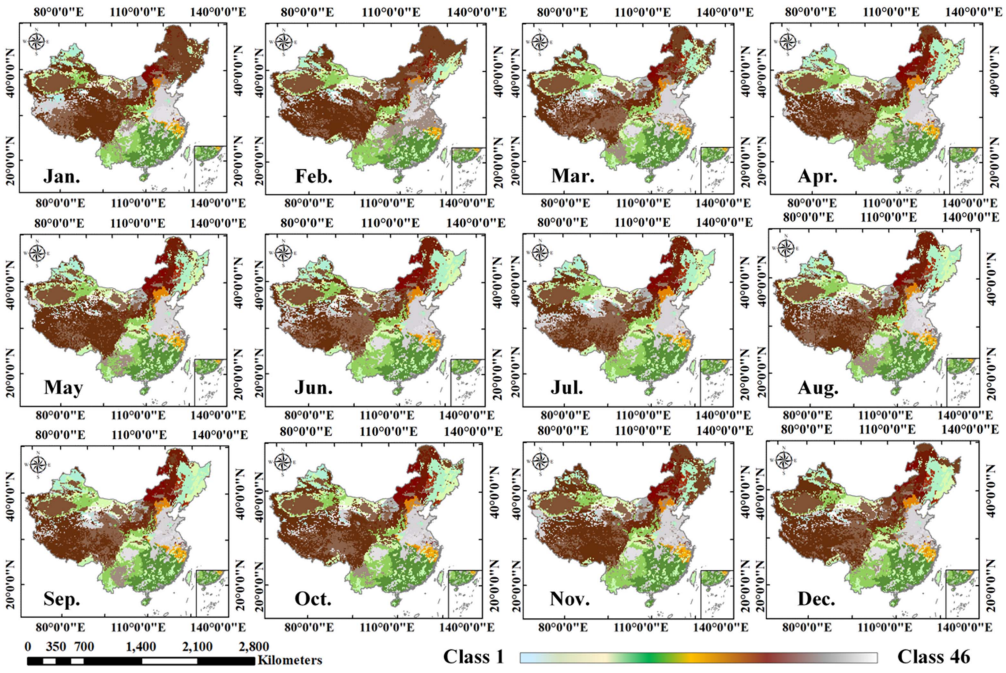

Fig. 8. Diagram of the daily changed RA-PLST-SM land environment. Providing the classification maps for the 15th day of each month.

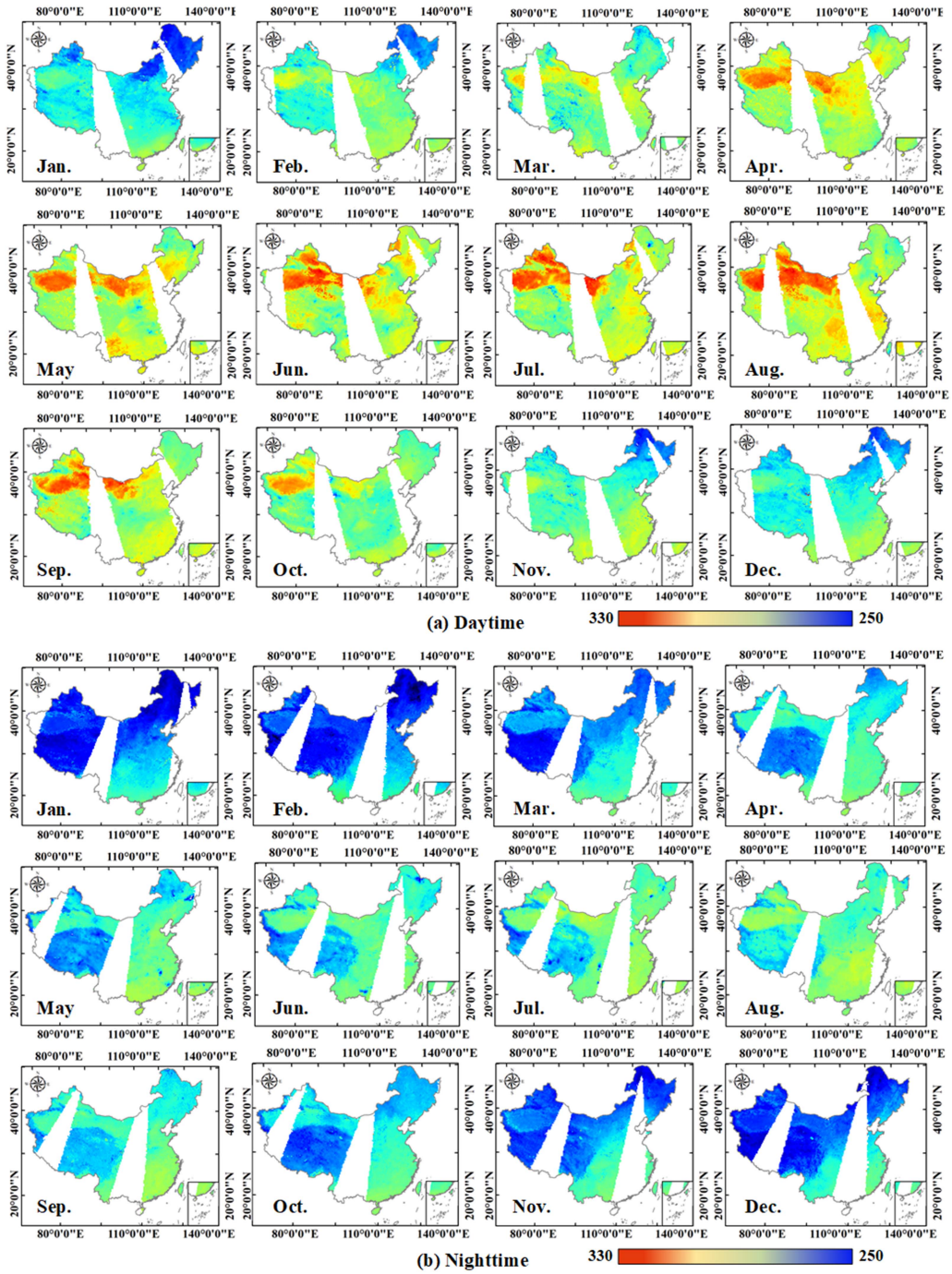

Fig. 9. RA-PLST-SM LSTs of the 15th day of each month. (a) Retrieving LSTs in the daytime. (b) Retrieving LSTs in the nighttime.

winter, a smaller angle of sunlight incidence results in shorter hours of daylight. Hence, less heat is absorbed by the surface, which causes too much LST variation under different land conditions, as different regions present unique heat budget properties. Overall, the LST results of RA-PLST-SM are presented with good accuracy, which can provide data support for other related applications.

2) Results Compared With TRIMS LSTs: Due to the large areas of missing data on MODIS LSTs each year, it is hard to assess the quality of ground temperature at an all-weather time scale. Hence, we selected the TRIMS temperature product to further evaluate the RA-PLST-SM results. We randomly extract 5% pixels from each day to complete the validation. One thing that needs to be noted is that there are still errors between the temperature product and MODIS, so this verification is only an indirect method because of the absence of true values under the cloud. To eliminate errors as much as possible, we first use the standard deviation of MODIS LST calculated with the physical annual temperature cycle [47] model to filter outliers in TRIMS. Then, adopting the same method as in the MODIS LST-based

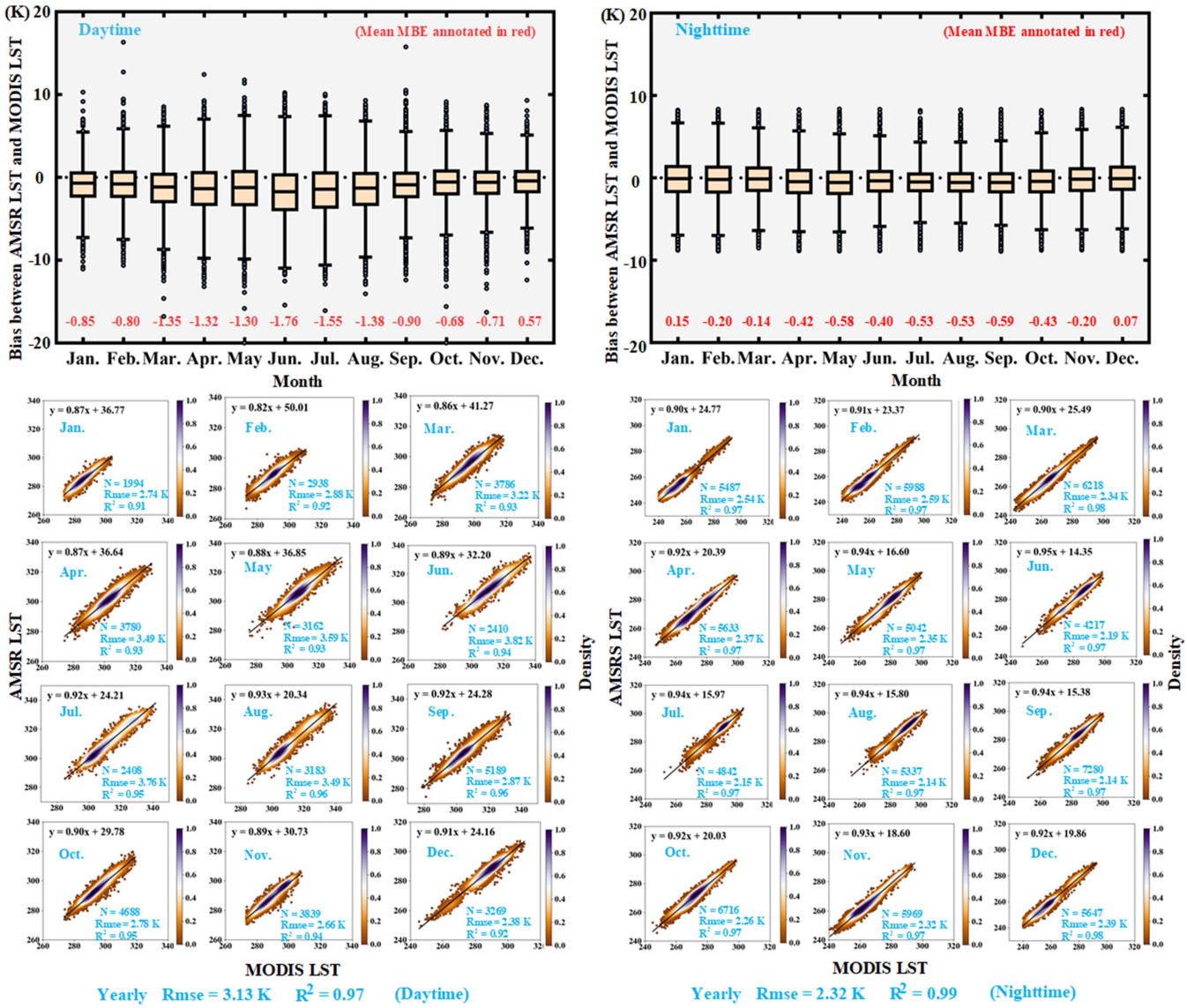

Fig. 10. Results of MBE, RMSE, and R^2 compared between RA-PLST-SM LST and MODIS LST.

validation to verify the accuracy of RA-PLST-SM. Fig. 11 shows the results of the comparison, which demonstrate a yearly average STD of 4.12 and 2.48 K at the daytime and nighttime. According to the STD (day/night) of 1.45 and 1.17 K between TRIMS LSTs and MODIS LSTs, the results of RA-PLST-SM LSTs have an available precise to obtain the LST data.

One thing that needs to be noted is the large amount of cloud cover on mainland China in summer, especially in July and August. This situation may be the reason why the larger error range appeared in summer. By contrast, the LST obtained via RA-PLST-SM can reach more than 0.9 in the metric of R^2 with TRIMS LST product, indicating that such a method owned a certain usability that can provide support to fill the nondata TIR-based LSTs due to the cloudy sky.

3) Assessment Based on In Situ Measurements: For the purpose of verifying the consistency of the actual LST, we acquired six meteorological stations to validate the RA-PLST-SM LST. Before the validation, considering the station LST is the point data in which it is hard to make a comparison with raster data, we also use a "3-σ" standard deviation between MODIS LSTs and station LSTs to filter the abnormal values. The results of each station, as shown in Fig. 12, indicate that the range of RMSE obtained 3.30–4.98 K in the daytime (mean RMSE is 4.54 K) and 2.91–4.10 K at the nighttime (mean RMSE is 3.48 K). And the metric of R^2 according to all selected in-situ stations illustrates that 0.85–0.98 (mean R^2 is 0.92) and 0.94–0.98 (mean R^2 is 0.96) respectively from daytime and nighttime.

C. Comparison With Existing Algorithms

Two existing methods that are used to retrieve PMW-based LST are adopted to make a comparison with our method, CCSEV [23] and TL-LUT [18]. Actually, these two methods are the typical studies on LST retrieval, which are based on the regression

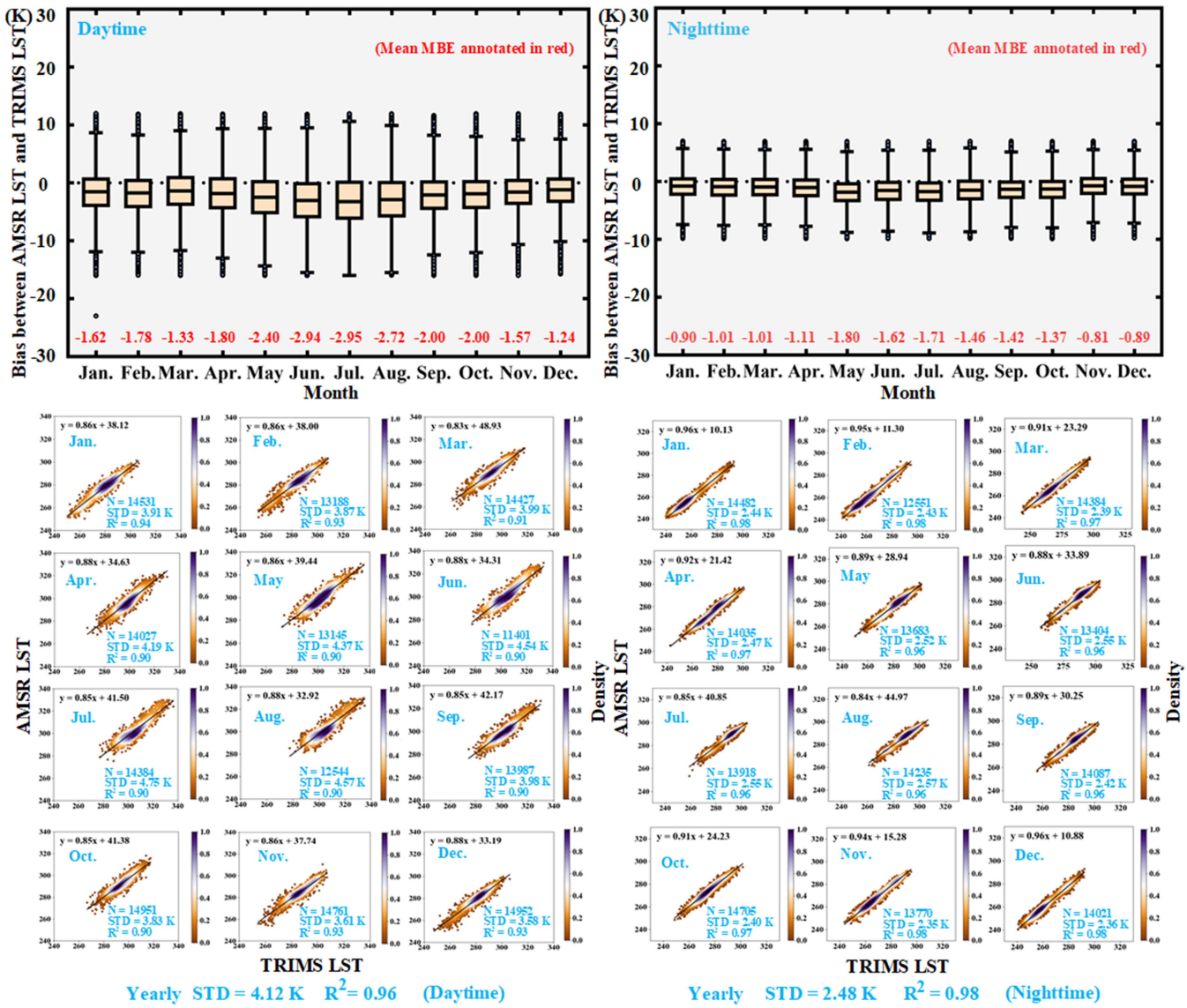

Fig. 11. Results of MBE, STD, and R^2 compared between RA-PLST-SM LST and TRIMS LST.

of underlying description. Of these two methods, TL-LUT proposed a lookup table method that can choose suitable regressed coefficients for different land-cover types. CCSEV completes the LST retrieval by further coupling land cover with landform. Subsequently, we propose a new method incorporating SM into the land cover and landform, which is a progress inspired by two previous studies. Consequently, TL-LUT and CCSEV are two techniques that have strong comparability with RA-PLST-SM.

In this section, we use MODIS LST and meteorological stations to achieve the comparison, as these two data sources are commonly used as the truth value to test the proposed method. The results of the comparison between RA-PLST-SM and two compared methods via MODIS LST are shown in Table III. According to the results, the method proposed in this article has an annual RMSE of 3.13 K in the daytime, which is 11.58% higher than 3.54 K of CCSEV and 17.85% higher than 3.81 K of TL-LUT. At nighttime, the proposed method has an annual RMSE of 2.32 K, which is improved by 12.12% to 2.64 K of CCSEV and 18.31% to 2.84 K of TL-LUT. In addition, the method proposed in this article also shows better performance than the other two comparison methods in each quarter, which also demonstrates that adding SM information is effective for PMW-based LST retrieval. The reason for this situation may be that the integration with SM can effectively separate its influence on microwave BT so that the regression coefficients obtained more accurately reflect the characteristics of LST. Moreover, the CCSEV, which further fused with landform, also refined the environment to achieve better accuracy. And the TL-LUT is less considered geographic heterogeneity; hence, the results will be presented with a lower accuracy by contrast to the other two methods.

Furthermore, we explicitly discuss the performance differences among each land-cover type. Since the types of shrublands and permanent snow and ice are extracted from a small number

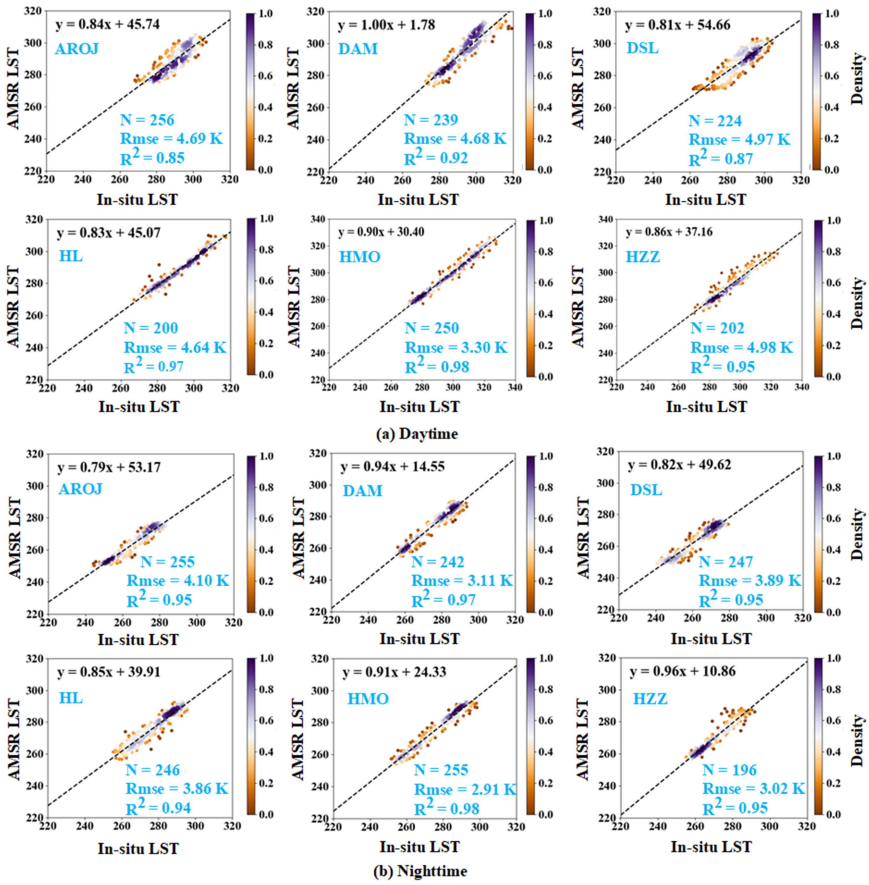

Fig. 12. Comparison between RA-PLST-SM LST and in situ LST from six meteorological stations. (a) Results of daytime. (b) Results of nighttime.

TABLE III
METRIC RESULTS BETWEEN RA-PLST-SM AND TWO EXISTING METHODS BASED ON MODIS LST

Time	Model	Spring (RMSE) R^2	Summer (RMSE) R^2	Autumn (RMSE) R^2	Winter (RMSE) R^2	Yearly (RMSE) R^2
Daytime	CC	(3.76) 0.92	(3.72) 0.93	(3.43) 0.95	(3.25) 0.88	(3.54) 0.96
	TL	(3.87) 0.89	(3.68) 0.93	(3.88) 0.91	(3.77) 0.74	(3.81) 0.95
	SM	**(3.43) 0.95**	**(3.68) 0.95**	**(2.78) 0.97**	**(2.66) 0.93**	**(3.13) 0.97**
Nighttime	CC	(2.69) 0.97	(2.41) 0.96	(2.57) 0.97	(2.93) 0.96	(2.64) 0.98
	TL	(2.87) 0.94	(2.82) 0.94	(2.87) 0.95	(2.77) 0.94	(2.84) 0.97
	SM	**(2.35) 0.98**	**(2.16) 0.97**	**(2.23) 0.98**	**(2.51) 0.97**	**(2.32) 0.99**

Note: SM is RA-PLST-SM; CC represents CCSEV; TL denotes TL-LUT. MBE and RMSE unit: K.
The bold results indicate that the proposed method has better accuracy.

of available MODIS pixels, we integrate the shrublands into savannas and grasslands, and combine the permanent snow and ice into the type of barren. After that, each model exhibits distinct characteristics on different surface types regardless of daytime and nighttime, as shown in Fig. 13. Concerning the RA-PLST-SM, the retrieval model shows decreased performance on barren and water bodies compared with the other types on both daytime and nighttime. The performance ranking of daytime RA-PLST-SM on each land-cover type is deciduous forests > croplands > savannas and grasslands > evergreen forests > barren > water bodies, and the nighttime is croplands > evergreen forests > deciduous forests > savannas and grasslands > water bodies > barren. For the CCSEV, the results illustrate evergreen forests > deciduous forests > croplands > savannas and grasslands > barren > water bodies, and barren > croplands > evergreen forests > savannas and grasslands > deciduous forests > water bodies in the daytime and nighttime, respectively. Although this method also demonstrates the phenomenon that the accuracy of barren is lower than the vegetation coverage types in the daytime, the accuracy of this land type at nighttime is better than croplands, evergreen forests, savannas and grasslands, and deciduous forests. Even so, this situation does not indicate that the performance in barren improved at nighttime but should be the fact that the performance in vegetation cover types decreased

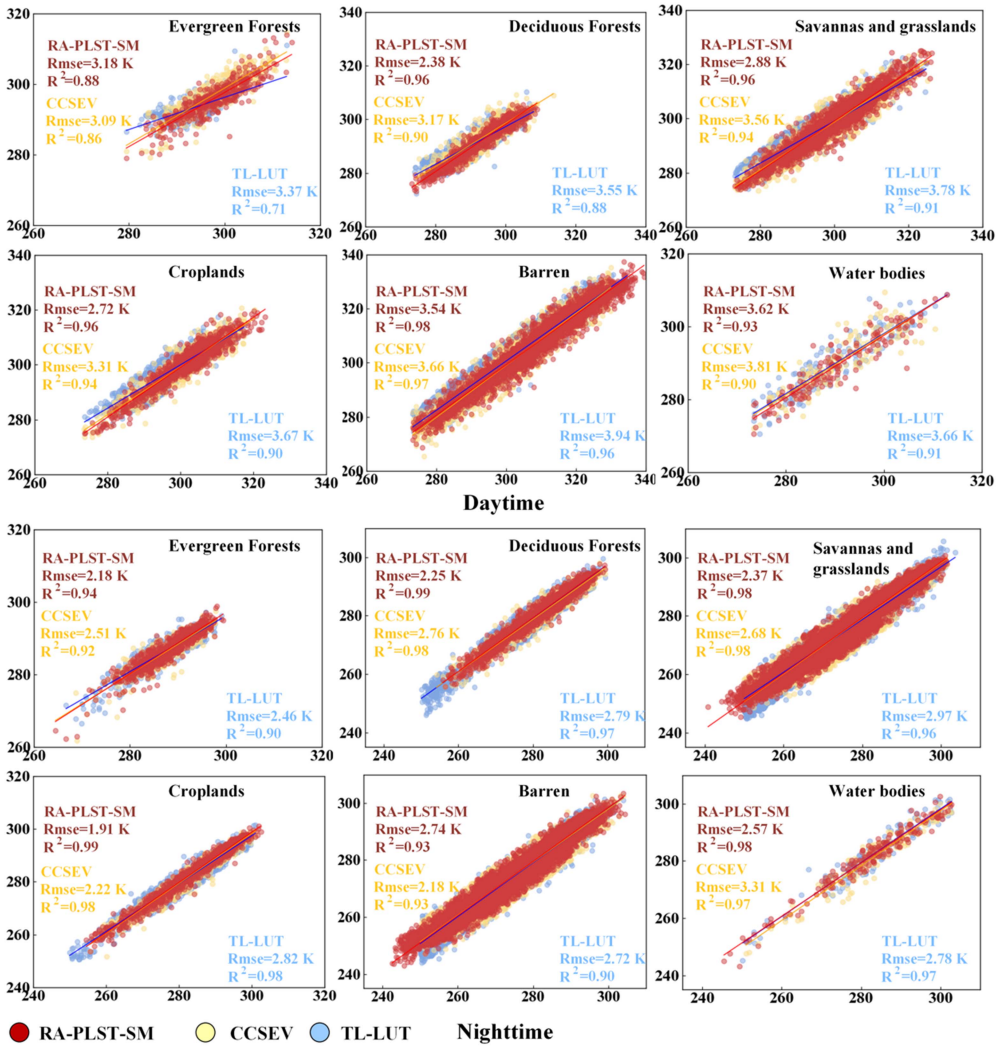

Fig. 13. Performance of RA-PLST-SM and two existing methods based on MODIS LSTs under each land-cover type.

in the daytime. The reason may be due to evergreen vegetation showing no performance degradation but having an impact on the type of deciduous vegetation, leading to the adequate account for seasonal changes. In particular, the temperature fluctuation caused by deciduous vegetation may be more pronounced at night than during the day, as the ground surface absorbs solar energy to stabilize the temperatures. According to the results of TL-LUT, the land types present a rank of evergreen forests > deciduous forests > water bodies > croplands > savannas and grasslands > barren at the daytime, and evergreen forests > barren > water bodies > deciduous forests > croplands > savannas and grasslands at the nighttime.

In particular, the RA-PLST-SM LSTs of evergreen forests illustrate a slightly lower accuracy than CCSEV in the daytime. The reason for this phenomenon may be that the evergreen forests have a cooling effect on skin temperatures; it is hard to characterize this effect through evapotranspiration after considering SM. Simultaneously, it will refine the vegetation type in the RA-PLST-SM land description, preventing the extraction of training data. Moreover, one thing that needs to be noted is that the accuracy of barren from RA-PLST-SM is not as good as other types in the nighttime. The factors that affect the performance in barren may be the different materials (or emissivity) of the land surface resulting in the diversity of heat absorption. Actually, we combine several land-cover types into the barren, including cities, deserts, and bare soil, presenting an intense influence by human activities and meteorological conditions in the nighttime. Also, uneven distribution of SM perhaps causes different thermal inertia for the capacity of heat storage from land. For instance, the soil with less water content will cause this region to cool down more rapidly at night due to the lower thermal inertia. Because the classification system of RA-PLST-SM lacks a description of these impermeable surfaces and dry areas, the LSTs retrieved from this category appear a decreased status in robustness. By contrast, the land surface is continuously heated during the day, which is subject to less external interference. Additionally, the overclassification of land scenarios on which SM is based is also one of the reasons why the RA-PLST-SM is inferior to the other two methods, as the barren cannot retain enough samples to obtain the coefficients.

TABLE IV
COMPARISON RESULTS OF SIX IN SITU MEASUREMENTS

Time	Station	MBE	RMSE	R^2
		SM (CC) TL	SM (CC) TL	SM (CC) TL
Daytime	AROJ	–0.60 (–0.79) 1.74	**4.69** (5.98) 4.88	0.85 (0.76) 0.84
	DAM	1.71 (2.55) 0.77	**4.68** (5.60) 5.51	0.92 (0.89) 0.86
	DSL	1.17 (1.25) 2.25	**4.97** (5.23) 5.65	0.87 (0.87) 0.86
	HL	–3.20 (–0.68) –0.06	**4.40** (4.69) 4.93	0.98 (0.93) 0.91
	HMO	0.73 (2.81) 1.27	**3.30** (4.19) 4.36	0.98 (0.98) 0.97
	HZZ	–3.00 (–0.55) –1.12	**4.50** (4.80) 4.87	0.96 (0.93) 0.90
Nighttime	AROJ	–2.14 (–0.75) 2.32	**4.10** (4.44) 4.27	0.95 (0.91) 0.94
	DAM	–1.11 (–0.32) –0.36	**3.11** (3.90) 4.44	0.97 (0.94) 0.92
	DSL	1.55 (1.70) 3.72	**3.89** (4.36) 4.93	0.95 (0.93) 0.95
	HL	–0.92 (0.72) –1.70	**3.86** (4.49) 4.90	0.94 (0.92) 0.91
	HMO	–0.47 (0.32) –0.32	**2.91** (3.82) 3.94	0.98 (0.96) 0.95
	HZZ	–0.43 (–0.94) –0.41	**3.02** (3.67) 3.83	0.95 (0.93) 0.91

Note: SM is RA-PLST-SM; CC represents CCSEV; and TL denotes TL-LUT. MBE and RMSE unit: K. The bold results indicate that the proposed method has better accuracy.

Moreover, we also adopt the LSTs from six meteorological stations to compare the performance differences of each method. Here, we utilize the broadband emissivity of MODIS to calculate the LST of the sites, so there exists a bias between the computed LSTs and actual LSTs. Based on this, MODIS LST is used to eliminate abnormal LSTs via the "3-σ" standard deviation. The results are shown in Table IV. It can be seen from the results that the method in this article shows a performance that is more consistent with the actual LSTs. It is worth mentioning that the MBE of RA-PLST-SM in HZZ and HL during the daytime is larger than the other stations, which is -3.2 K and -3.0 K, respectively. This situation may be related to the representativeness of the station data at the 25 km resolution of PMW LST. Of them, HZZ is a desert site, which is only 2 km away from the farmland in the north [48]. Therefore, its pixel temperature mainly contains the SM characteristics of the farmland, resulting in its lower verification accuracy. HL is close to the reservoir, which causes the pixels containing it to be LST retrieved based on the water scenario, thus affecting the fluctuation of MBE. Elevation is the main influencing factor of DSL and AROJ. Although they have better spatial representativeness with smaller fluctuation of MBE, the accuracy of RMSE is still lower than the HZZ and HL. DAM is a farmland station, but there are large areas of Gobi and desert around it, and the distance is no more than 10 km. Therefore, the data observations of RA-PLST-SM will cover a part of the high-temperature surface of the Gobi and desert, resulting in lower MBE and RMSE results. Moreover, the HMO station is located in the desert area in the lower reaches of the Heihe River, with only sparse natural oases, which is the most representative of the real land scene, so the RMSE result performs best.

As for the nighttime, the LST in AROJ and DSL is relatively lower than the other stations, due to both elevations being above 3000 m. Additionally, the airflow in diverse terrains contained in the 25 km pixel will lead to different dissipation rates of heat storage incoming from the daytime. In consequence, the RMSE and MBE present lower results in the nighttime. For the stations of DAM and HZZ, the location is closer to AROJ and DSL, but the elevation is about 1500 m, so the accuracy of these two stations is relatively better than AROJ and DSL. Because the pixels of DAM station cover Gobi and desert, the RMSE of DAM is inferior to the HZZ. Reservoirs usually release heat at night due to the lack of solar radiation. Accordingly, this phenomenon may be the primary reason for poor RMSE in HL. The assessment results of HMO are still stable in the nighttime because of its good representativeness.

In order to show the LST trend of each method and in situ data, this article provides daily LST fluctuations, as shown in Fig. 14. It can also be seen from the results that the results of RA-PLST-SM can maintain the trend consistency with the measured LST. In contrast, LST fluctuates more sharply during the day and more gently at night, which is consistent with previous accuracy verification results. In addition, the missing data on partial dates is the reason for the gaps appearing in graphs.

V. DISCUSSIONS

A. Difference Among Time-Interval-Based Models

Different time intervals determine the training samples of a regression model. Generally, the longer time interval can extract more available values to assist the model in acquiring appropriate parameters. Even so, environmental variables may include more uncertain changes over longer periods, such as the change of seasons, the evolution of vegetation phenology, and diverse meteorological situations. Therefore, how to find the tradeoff between the number of training samples and the appropriate time interval is essential to work for the retrieval of microwave-based LST.

In this section, the MODIS LST is used to achieve the comparison experiments. There are three reasons for choosing this LST data for verification: first, the MODIS data are raster data, which facilitates the discussion of accuracy differences with the retrieved LST at a grid scale; second, MODIS LST is retrieved based on the thermal infrared sensor, which has strong

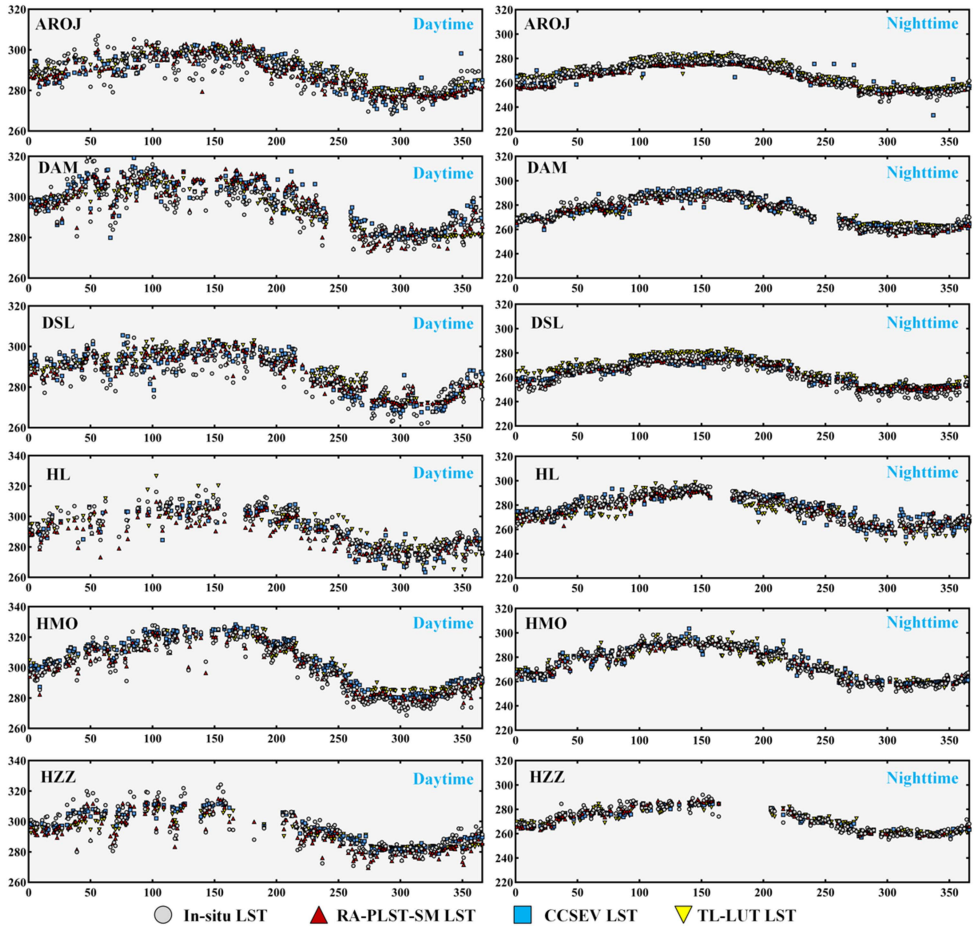

Fig. 14. Daily LST trends among the in situ measurements, RA-PLST-SM, and two comparison methods.

consistency with the actual LST because thermal infrared is intensely related to heat; third, MODIS LST is wide as truth LST used in a large number of studies. On this basis, we further compare the variability in error/bias between the models on the time scale of month, quarter, annual, and even the fusion model in accordance with three-time scales. For the convenience of description, we call the models based on months, quarters, years, and fusion, respectively, as MM, QM, YM, and FM. The comparison results are shown in Fig. 15.

Obviously, the results show that the FM model shows good accuracy in both daytime and nighttime because it fully integrates the advantages of different time-scale models. In addition, the performance of the YM model is the worst, which is directly related to the serious confusion caused by the data covering the whole year. At the same time, the SM model has better accuracy than the MM model among all the daytime results. All in all, the monthly accuracy comparison illustrates that the metric ranking of each model should be FM > QM > MM > YM in the daytime and nighttime. In general, the sky is often heavily obscured by clouds and fog, and the regression data that can be extracted are minimal, so the accuracy of the MM model is poor. As for the YM, different seasonality is the main reason for the degradation of model performance, such as the replacement of vegetation phenology and changes in climate at different latitudes. These situations will directly make it hard for the obtained regression coefficients to relate to the geographical environment at different time scales closely.

For the FM model, the validated results are shown best among all compared time intervals. Coupling the LSTs with the best accuracy from monthly, quarterly, and yearly model is the main reason for this situation. According to the fusion strategy of FM, the model first extracts the LSTs with outstanding RMSE estimation from MM, QM, and YM, in line with the monthly scale, as the smaller time interval may present great coefficients to predict the precise data. Subsequently, we further fill the no-data pixels via quarter scale, which is stepwise padding the LST data into the results. In the next step, we use this strategy to further couple the year scale to generate an all-weather LST. Through these three steps, the retrieved results that are coincident with MODIS LST will remain in the final LST data, which is the reason for gaining the best assessment results among the other three models.

B. *Sensibility of the Compensate Components*

Whether there is a difference in retrieval accuracy between the two environmental compensation components is an issue that needs to be discussed. The two components include the correction of atmospheric water vapor and soil compensation for long-term agricultural wetness. Simultaneously, we use

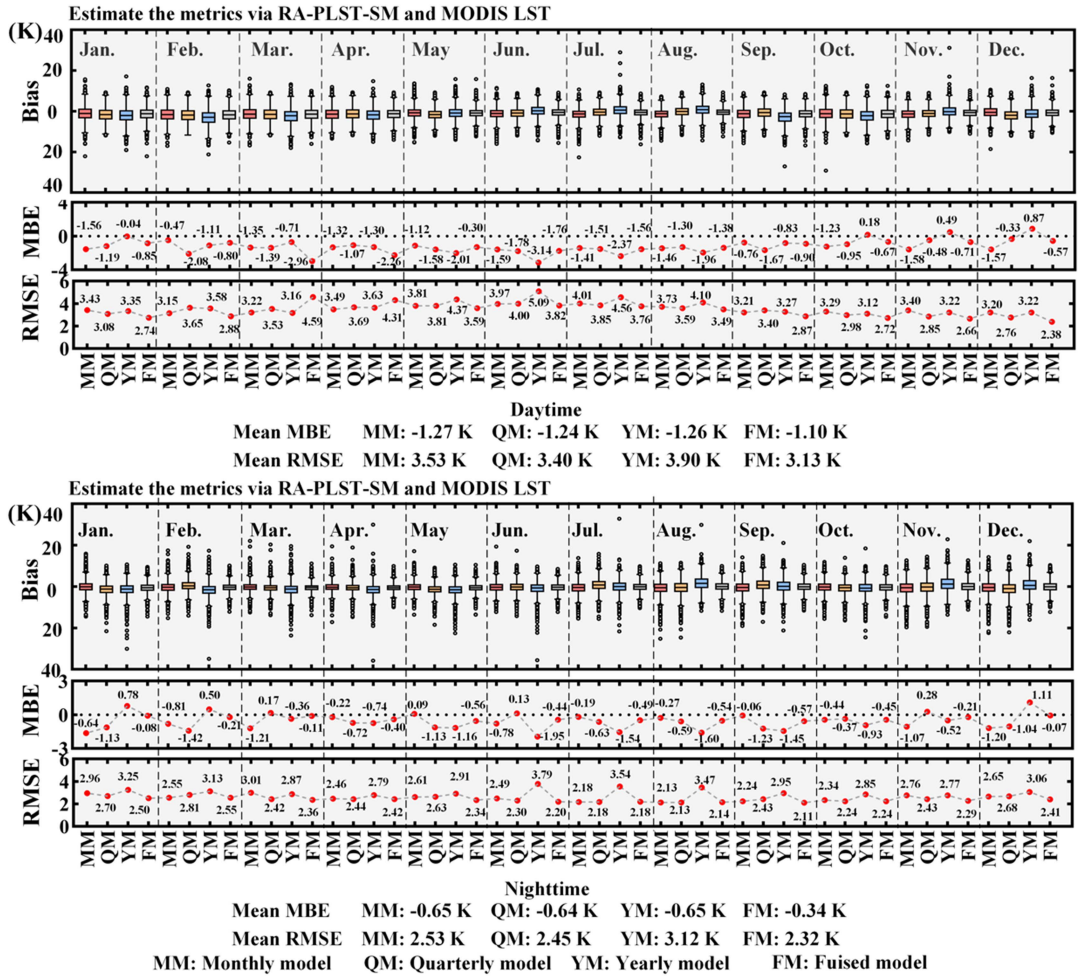

Fig. 15. Comparison of each time-interval-based model based on MODIS LSTs.

TABLE V
PERFORMANCE DIFFERENCE OF TWO COMPENSATE COMPONENTS IN THE RETRIEVAL EQUATION

Time	Model	Spring (RMSE) R^2	Summer (RMSE) R^2	Autumn (RMSE) R^2	Winter (RMSE) R^2	Yearly Average (RMSE) R^2
Daytime	CA	(3.55) 0.94	(3.80) 0.95	(3.13) 0.96	(3.21) 0.90	(3.42) 0.94
	CM	(3.57) 0.94	(3.81) 0.95	(3.14) 0.96	(3.21) 0.90	(3.43) 0.94
	NC	(3.58) 0.94	(3.82) 0.95	(3.15) 0.96	(3.24) 0.90	(3.45) 0.94
	AL	(3.53) 0.94	(3.79) 0.95	(3.11) 0.96	(3.18) 0.90	(3.40) 0.94
Nighttime	CA	(2.76) 0.96	(2.47) 0.96	(2.62) 0.97	(2.93) 0.96	(2.70) 0.96
	CM	(2.78) 0.96	(2.42) 0.96	(2.62) 0.97	(2.94) 0.96	(2.69) 0.96
	NC	(2.81) 0.96	(2.47) 0.96	(2.62) 0.97	(2.95) 0.96	(2.71) 0.96
	AL	(2.69) 0.97	(2.39) 0.96	(2.56) 0.97	(2.91) 0.97	(2.63) 0.97

Note: CA: only considering the correction of atmosphere water vapor; CM: only considering moist soil compensation; NC: not considered both of them; and AL: considering both ones. RMSE unit: K

the quarterly model to complete the comparison. The reason for the choice of this model mainly includes two aspects: first, quarter models have a relatively stable performance; second, the quarterly model allows us to focus on seasonal differentiation.

The comparison results are shown in Table V. According to the results, atmospheric correction plays a greater function than wet soil compensation in the daytime, which is closely related to the fact that clouds/fog often commonly appear to affect the PMW BT during the day. Additionally, we can see

that a correlation existed between SM and atmospheric water vapor because there is consistency in the effectiveness of the two compensation components. Moreover, the results also manifest that the performance of the LST retrieval model can be significantly improved under the combined effect of two compensations.

VI. Conclusion

PMW-based LST is a crucial source that complements to fill the cloudy severe data missing from TIR. Nonetheless, the water content of the land directly affects the emissivity, which is a majority physical variable for LST in accordance with the PMW-based RTE; yet the existing studies less consider this parameter. Therefore, the main effort of this article is to verify the effectiveness of a dynamic land description that incorporates SM to retrieve the PMW-based LST. The results also demonstrate that the proposed technique, which incorporates SM, is effective for LST retrieval. This article tested the methods via MODIS LSTs, advanced LST product, and in situ measurements, respectively. The results show that the proposed RA-PLST-SM method can obtain annual RMSE of 3.13 K and 2.32 K in the daytime and nighttime, which improves 0.41 K and 0.68 K compared with two advanced techniques in the daytime, and 0.32 K and 0.52 K in the nighttime. The accuracy of RA-PLST-SM based on advanced LST product shows an annual STD of 4.12 K/2.48 K on the results during day/night. Additionally, RA-PLST-SM has better consistency with the in situ LSTs from six meteorological stations. Moreover, the time fusion strategy we proposed has been verified to be effective and has better performance than the monthly, quarterly, and annual models. Furthermore, we validate the sensitivity of the two components in the retrieval equation: atmospheric correction and moist soil compensation. The results illustrate that the atmospheric correction plays a stronger role during the day, and the model can gain better LST results via the cooperative effects of the two compensations.

Some limitations will be our future work. First, how to consider weather conditions is one of the directions we need to explore in the future. Second, which retrieval means (linear models or machine-learning-based models) are suitable for which terrestrial scene is also a critical work we need to explore further.

Acknowledgment

The authors would like to thank the anonymous reviewers for helping to improve this article.

References

[1] I. Sandholt, K. Rasmussen, and J. Andersen, "A simple interpretation of the surface temperature/vegetation index space for assessment of surface moisture status," *Remote Sens. Environ.*, vol. 79, no. 2/3, pp. 213–224, Feb. 2002.

[2] S.-B. Duan et al., "Influence of adjacency effect on high-spatial-resolution thermal infrared imagery: Implication for radiative transfer simulation and land surface temperature retrieval," *Remote Sens. Environ.*, vol. 245, Aug. 2020, Art. no. 111852.

[3] M. Taheri, A. Mohammadian, F. Ganji, M. Bigdeli, and M. Nasseri, "Energy-based approaches in estimating actual evapotranspiration focusing on land surface temperature: A review of methods, concepts, and challenges," *Energies*, vol. 15, no. 4, Feb. 2022, Art. no. 1264.

[4] A. Shalishe, A. Bhowmick, and K. Elias, "Agricultural drought analysis and its association among land surface temperature, soil moisture and precipitation in Gamo Zone, Southern Ethiopia: A remote sensing approach," *Natural Hazards*, vol. 117, no. 1, pp. 57–70, May 2023.

[5] U. Mazhar, S. Jin, T. Hu, M. Bilal, M. A. Ali, and L. Atique, "Long-time variation and mechanism of surface energy budget over diverse geographical regions in Pakistan," *IEEE J. Sel. Topics Appl. Earth Observ. Remote Sens.*, vol. 15, pp. 5203–5213, Jun. 2022.

[6] T.-L. Chen, H. Lin, and Y.-H. Chiu, "Heat vulnerability and extreme heat risk at the metropolitan scale: A case study of Taipei metropolitan area, Taiwan," *Urban Climate*, vol. 41, Jan. 2022, Art. no. 101054.

[7] H. Sun, Z. Xu, and H. Liu, "An evaluation of the response of vegetation greenness, moisture, fluorescence, and temperature-based remote sensing indicators to drought stress," *J. Hydrol.*, vol. 625, Oct. 2023, Art. no. 130125.

[8] H. Sun, J. Gao, T. Yan, K. Hu, and Z. Xu, "Remote sensing of vegetation drought: Current situation and prospects," *Nat. Remote Sens. Bull.*, pp. 1–18, 2024.

[9] H. Sun et al., "Agricultural drought dynamics in China during 1982–2020: A depiction with satellite remotely sensed soil moisture," *GIScience Remote Sens.*, vol. 60, no. 1, Dec. 2023, Art. no. 2257469.

[10] D. Cho, D. Bae, C. Yoo, J. Im, Y. Lee, and S. Lee, "All-sky 1 km MODIS land surface temperature reconstruction considering cloud effects based on machine learning," *Remote Sens.*, vol. 14, no. 8, Apr. 2022, Art. no. 1815.

[11] S.-B. Duan, Y. Lian, E. Zhao, H. Chen, W. Han, and Z. Wu, "A novel approach to all-weather LST estimation using XGBoost model and multisource data," *IEEE Trans. Geosci. Remote Sens.*, vol. 61, Oct. 2023, Art. no. 5004614.

[12] L. Wei, H. Wu, X.-G. Jiang, C. Ru, Y.-Z. Jiang, and C.-X. Gao, "A modified single-channel algorithm for estimating land surface temperature from UAV TIR imagery," in *Proc. IEEE Int. Geosci. Remote Sens. Symp.*, Brussels, Belgium, 2021, pp. 8185–8188.

[13] Z. Qin, A. Karnieli, and P. Berliner, "A mono-window algorithm for retrieving land surface temperature from Landsat TM data and its application to the Israel-Egypt border region," *Int. J. Remote Sens.*, vol. 22, no. 18, pp. 3719–3746, Jan. 2001.

[14] A. Gillespie, S. Rokugawa, T. Matsunaga, J. S. Cothern, S. Hook, and A. B. Kahle, "A temperature and emissivity separation algorithm for advanced spaceborne thermal emission and reflection radiometer (ASTER) images," *IEEE Trans. Geosci. Remote Sens.*, vol. 36, no. 4, pp. 1113–1126, Jul. 1998.

[15] C. Coll et al., "Temperature and emissivity separation from ASTER data for low spectral contrast surfaces," *Remote Sens. Environ.*, vol. 110, no. 2, pp. 162–175, Sep. 2007.

[16] K. Mao et al., "A general paradigm for retrieving soil moisture and surface temperature from passive microwave remote sensing data based on artificial intelligence," *Remote Sens.*, vol. 15, no. 7, Mar. 2023, Art. no. 1793.

[17] P. Wu et al., "A two-step deep learning framework for mapping gapless all-weather land surface temperature using thermal infrared and passive microwave data," *Remote Sens. Environ.*, vol. 277, Aug. 2022, Art. no. 113070.

[18] J. Zhou, F. Dai, X. Zhang, S. Zhao, and M. Li, "Developing a temporally land cover-based look-up table (TL-LUT) method for estimating land surface temperature based on AMSR-E data over the Chinese landmass," *Int. J. Appl. Earth Observ. Geoinf.*, vol. 34, pp. 35–50, Feb. 2015.

[19] P. Fu, Y. Xie, Q. Weng, S. Myint, K. Meacham-Hensold, and C. Bernacchi, "A physical model-based method for retrieving urban land surface temperatures under cloudy conditions," *Remote Sens. Environ.*, vol. 230, Sep. 2019, Art. no. 111191.

[20] M. J. McFarland, R. L. Miller, and C. M. U. Neale, "Land surface temperature derived from the SSM/I passive microwave brightness temperatures," *IEEE Trans. Geosci. Remote Sens.*, vol. 28, no. 5, pp. 839–845, Sep. 1990.

[21] E. Zhao, C. Gao, X. Jiang, and Z. Liu, "Land surface temperature retrieval from AMSR-E passive microwave data," *Opt. Exp.*, vol. 25, no. 20, Oct. 2017, Art. no. A940.

[22] S.-B. Duan et al., "Land surface temperature retrieval from passive microwave satellite observations: State-of-the-art and future directions," *Remote Sens.*, vol. 12, no. 16, Aug. 2020, Art. no. 2573.

[23] Q. Zhang and J. Cheng, "An empirical algorithm for retrieving land surface temperature from AMSR-E data considering the comprehensive effects of environmental variables," *Earth Space Sci.*, vol. 7, no. 4, Apr. 2020, Art. no. e2019EA001006.

[24] Q. Zhang, N. Wang, Y. Wu, and A. Chen, "Adapting an existing empirical algorithm for microwave land surface temperature retrieval in China for AMSR2 data," *Remote Sens.*, vol. 15, no. 13, Jun. 2023, Art. no. 3228.
[25] M. Owe and A. A. Van De Griend, "On the relationship between thermodynamic surface temperature and high-frequency (37 GHz) vertically polarized brightness temperature under semi-arid conditions," *Int. J. Remote Sens.*, vol. 22, no. 17, pp. 3521–3532, Jan. 2001.
[26] H. Sun, X. Zhang, and X. Zhao, "Series or parallel? An exploration in coupling physical model and machine learning method for disaggregating satellite microwave soil moisture," *IEEE Trans. Geosci. Remote Sens.*, vol. 60, Oct. 2022, Art. no. 4415015.
[27] J. T. Trok, F. V. Davenport, E. A. Barnes, and N. S. Diffenbaugh, "Using machine learning with partial dependence analysis to investigate coupling between soil moisture and near-surface temperature," *J. Geophys. Res. Atmos.*, vol. 128, no. 12, Jun. 2023, Art. no. e2022JD038365.
[28] H. Sun and J. Gao, "A pixel-wise calculation of soil evaporative efficiency with thermal/optical remote sensing and meteorological reanalysis data for downscaling microwave soil moisture," *Agricultural Water Manage.*, vol. 276, Feb. 2023, Art. no. 108063.
[29] Z. Wan, "New refinements and validation of the MODIS land-surface temperature/emissivity products," *Remote Sens. Environ.*, vol. 112, no. 1, pp. 59–74, Jan. 2008.
[30] M. A. Friedl et al., "MODIS Collection 5 global land cover: Algorithm refinements and characterization of new datasets," *Remote Sens. Environ.*, vol. 114, no. 1, pp. 168–182, Jan. 2010.
[31] Q. Zhang, Q. Yang, and C. Wang, "SRTM error distribution and its associations with landscapes across China," *Photogramm. Eng. Remote Sens.*, vol. 82, no. 2, pp. 135–148, Feb. 2016.
[32] Q. Li et al., "A 1 km daily soil moisture dataset over China using in situ measurement and machine learning," *Earth Syst. Sci. Data*, vol. 14, no. 12, pp. 5267–5286, Nov. 2022.
[33] Q. Li, G. Shi, and W. Shangguan, "A 1 km daily soil moisture dataset over China based on situ measurement (2000-2020))," National Tibetan Plateau Data Center, Boston, MA, USA, Dec. 6, 2022.
[34] J. Wang, "The map of desert distribution in 1:2,000,000 in China (1974)," A Big Earth Data Platform for Three Poles, Jul. 4, 2013.
[35] L. Ding, X. Zhang, J. Zhou, W. Tang, X. Zhang, and M. A. J., "Daily 1-km all-weather land surface temperature dataset for the China's landmass and its surrounding areas (TRIMS LST; 2000-2022)," National Tibetan Plateau Data Center, Boston, MA, USA, Aug. 21, 2023.
[36] W. Tang et al., "TRIMS LST: A daily 1-km all-weather land surface temperature dataset for the China's landmass and surrounding areas (2000–2022)," *Earth Syst. Sci. Data*, vol. 16, no. 1, pp. 387–419, Jan. 2024.
[37] J. Zhou et al., "A thermal sampling depth correction method for land surface temperature estimation from satellite passive microwave observation over barren land," *IEEE Trans. Geosci. Remote Sens.*, vol. 55, no. 8, pp. 4743–4756, Aug. 2017.
[38] X. Zhang, J. Zhou, F.-M. Gottsche, W. Zhan, S. Liu, and R. Cao, "A method based on temporal component decomposition for estimating 1-km all-weather land surface temperature by merging satellite thermal infrared and passive microwave observations," *IEEE Trans. Geosci. Remote Sens.*, vol. 57, no. 7, pp. 4670–4691, Jul. 2019.
[39] X. Zhang, J. Zhou, S. Liang, and D. Wang, "A practical reanalysis data and thermal infrared remote sensing data merging (RTM) method for reconstruction of a 1-km all-weather land surface temperature," *Remote Sens. Environ.*, vol. 260, Jul. 2021, Art. no. 112437.
[40] X. Li et al., "Heihe watershed allied telemetry experimental research (HiWATER)," *Bull. Amer. Meteorol. Soc.*, vol. 94, pp. 1145–1160, 2013.
[41] T. Che et al., "Integrated hydrometeorological, snow and frozen-ground observations in the alpine region of the Heihe River Basin, China," *Earth Syst. Sci. Data*, vol. 11, no. 3, pp. 1483–1499, Sep. 2019.
[42] S. Liang, *Quantitative Remote Sensing of Land Surfaces*. Hoboken, NJ, USA: Wiley, 2004.
[43] J. Ma et al., "An atmospheric influence correction method for longwave radiation-based in-situ land surface temperature," *Remote Sens. Environ.*, vol. 293, Aug. 2023, Art. no. 113611.
[44] K. Moser, C. Ahn, and G. Noe, "Characterization of microtopography and its influence on vegetation patterns in created wetlands," *Wetlands*, vol. 27, no. 4, pp. 1081–1097, Dec. 2007.
[45] K. L. Wolf, C. Ahn, and G. B. Noe, "Microtopography enhances nitrogen cycling and removal in created mitigation wetlands," *Ecol. Eng.*, vol. 37, no. 9, pp. 1398–1406, Sep. 2011.
[46] W. Zhu, Y. Pan, H. He, L. Wang, M. Mou, and J. Liu, "A changing-weight filter method for reconstructing a high-quality NDVI time series to preserve the integrity of vegetation phenology," *IEEE Trans. Geosci. Remote Sens.*, vol. 50, no. 4, pp. 1085–1094, Apr. 2012.
[47] B. Bechtel, "Robustness of annual cycle parameters to characterize the urban thermal landscapes," *IEEE Geosci. Remote Sens. Lett.*, vol. 9, no. 5, pp. 876–880, Sep. 2012.
[48] W. Yu, M. Ma, Z. Li, J. Tan, and A. Wu, "New scheme for validating remote-sensing land surface temperature products with station observations," *Remote Sens.*, vol. 9, no. 12, Nov. 2017, Art. no. 1210.

Weizhen Ji received the B.S. degree in geographic information system from the School of Municipal and Geomatics Engineering, Hunan City University, Yiyang, China, in 2018, and the M.S. degree in cartography and geography information system from the School of Civil and Surveying and Mapping Engineering, Jiangxi University of Science and Technology, Ganzhou, China, in 2021. He is currently working toward the Ph.D. degree in cartography and geography information system with the State Key Laboratory of Remote Sensing Science, Faculty of Geographical Science, Beijing Normal University, Beijing, China.

His research interests include thermal remote sensing of urban environment and spatiotemporal downscaling of land surface temperature.

Yunhao Chen received the B.S. and M.S. degrees in resource management from the Anhui University of Science and Technology, Huainan, China, in 1994 and 1997, respectively, and the Ph.D. degree in geodetic engineering from the China University of Mining and Technology, Beijing, China, in 1999.

From 2000 to 2001, he was a Postdoctoral Researcher with Beijing Normal University, Beijing, China. Since 2001, he has been with the Faculty of Geographical Science, Beijing Normal University, where he is currently a Professor with the State Key Laboratory of Remote Sensing Science. His research interests include thermal remote sensing of urban environment and applications of remote sensing in ecology.

Han Gao received the B.S. degree in remote sensing science and technology from the College of Geoscience and Surveying Engineering, China University of Mining and Technology-Beijing, Beijing, China, in 2023. She is currently working toward the M.S. degree in cartography and geographic information system with the State Key Laboratory of Remote Sensing Science, Faculty of Geographical Science, Beijing Normal University, Beijing.

Her research interests include remote sensing of urban environment and spatiotemporal downscaling of land surface temperature.

Haiping Xia received the B.S. degree in geographic information system from the School of Environment Science and Spatial Informatics, China University of Mining and Technology, Xuzhou, China, in 2015, and the Ph.D. degree in cartography and geography information system from the Faculty of Geographical Science, Beijing Normal University, Beijing, China, in 2021.

She is currently with the Institute of Remote Sensing and Earth Sciences, Hangzhou Normal University, Hangzhou, China. Her research interests include thermal sharpening and analysis on urban thermal environment.